

## C: Plasmonics; Optical, Magnetic, and Hybrid Materials

**Improved Crystalline Structure and Enhanced Photoluminescence  
of ZnO Nanolayers in BiSe/ZnO Heterostructures**

Margarita Baitimirova, Jana Andzane, Roman Viter, Bernard Fraise, Octavio Graniel, Mikhael Bechelany, John Daniel Watt, Domantas Peckus, Sigitas Tamulevicius, and Donats Erts

*J. Phys. Chem. C*, **Just Accepted Manuscript** • DOI: 10.1021/acs.jpcc.9b08417 • Publication Date (Web): 02 Dec 2019

Downloaded from [pubs.acs.org](https://pubs.acs.org) on December 5, 2019

**Just Accepted**

“Just Accepted” manuscripts have been peer-reviewed and accepted for publication. They are posted online prior to technical editing, formatting for publication and author proofing. The American Chemical Society provides “Just Accepted” as a service to the research community to expedite the dissemination of scientific material as soon as possible after acceptance. “Just Accepted” manuscripts appear in full in PDF format accompanied by an HTML abstract. “Just Accepted” manuscripts have been fully peer reviewed, but should not be considered the official version of record. They are citable by the Digital Object Identifier (DOI®). “Just Accepted” is an optional service offered to authors. Therefore, the “Just Accepted” Web site may not include all articles that will be published in the journal. After a manuscript is technically edited and formatted, it will be removed from the “Just Accepted” Web site and published as an ASAP article. Note that technical editing may introduce minor changes to the manuscript text and/or graphics which could affect content, and all legal disclaimers and ethical guidelines that apply to the journal pertain. ACS cannot be held responsible for errors or consequences arising from the use of information contained in these “Just Accepted” manuscripts.

1  
2  
3  
4  
5  
6  
7 Improved Crystalline Structure and Enhanced Photoluminescence of  
8  
9  
10 ZnO Nanolayers in Bi<sub>2</sub>Se<sub>3</sub>/ZnO Heterostructures  
11  
12  
13

14 *Margarita Baitimirova<sup>1</sup>, Jana Andzane<sup>1</sup>, Roman Viter<sup>2</sup>, Bernard Fraisse<sup>4</sup>, Octavio Granie<sup>5</sup>,*

15 *Mikhael Bechelany<sup>5</sup>, John D. Watt,<sup>6</sup> Domantas Peckus<sup>7</sup>, Sigitas Tamulevicius<sup>7</sup>, Donats Erts<sup>1,3\*</sup>*  
16  
17  
18  
19  
20  
21  
22

23 <sup>1</sup>Institute of Chemical Physics, <sup>2</sup>Institute of Atomic Physics and Spectroscopy, and  
24

25  
26 <sup>3</sup>Department of Chemistry, University of Latvia, Raina Boulevard 19, LV 1586, Riga, Latvia  
27  
28  
29  
30

31 <sup>4</sup>Institute Charles Gerhardt, University of Montpellier, UMR 5253 CNRS-UM-ENSCM, Place  
32

33  
34 Eugene Bataillon, 34095, Montpellier, France  
35  
36  
37  
38

39 <sup>5</sup>European Institute of Membranes, University of Montpellier, CNRS, ENSCM, Place Eugene  
40

41  
42 Bataillon, 34095 Montpellier, France  
43  
44  
45  
46

47 <sup>6</sup>Center for Integrated Nanotechnologies, Los Alamos National Laboratory, Albuquerque, NM  
48  
49

50 87185-1315, US  
51  
52  
53  
54  
55

1  
2  
3  
4 <sup>7</sup>Institute of Materials Science, Kaunas University of Technology, K. Barsausko st. 59, LT-

5  
6  
7 51423, Kaunas, Lithuania

8  
9  
10  
11 \*E-mail: donats.erts@lu.lv

12  
13  
14  
15  
16 KEYWORDS: zinc oxide, bismuth selenide, photoluminescence, interface, nanostructures

17  
18  
19  
20  
21  
22  
23  
24  
25  
26 ABSTRACT

27  
28  
29 Bi<sub>2</sub>Se<sub>3</sub>/ZnO heterostructure is a new combination of high and low band gap nanomaterials that  
30  
31  
32 can be implemented for optoelectronic devices. Influence of the Bi<sub>2</sub>Se<sub>3</sub> substrate on  
33  
34  
35 crystallization of ZnO nanolayers and charge separation at the Bi<sub>2</sub>Se<sub>3</sub>/ZnO interface are  
36  
37  
38 important parameters, which affect optical and electronic properties of the heterostructure.  
39  
40  
41  
42  
43 Despite a few works on Bi<sub>2</sub>Se<sub>3</sub>/ZnO heterostructures, the mechanisms of enhanced optical  
44  
45  
46 properties and correlation between optical and structural properties in such heterostructures  
47  
48  
49 are not studied in detail. In the present paper, we report on structure and optical properties of  
50  
51  
52  
53  
54 ZnO nanolayers with different thicknesses (10-150 nm) deposited by atomic layer deposition

1  
2  
3 on planar and non-planar  $\text{Bi}_2\text{Se}_3$  nanostructured coatings. Crystallization of ZnO nanolayers  
4  
5  
6  
7 grown on  $\text{Bi}_2\text{Se}_3$  and Si substrates was analyzed by X-ray diffraction, Scanning and  
8  
9  
10 Transmission Electron Microscopy methods. Enhancement of ZnO photoluminescence in  
11  
12  
13  $\text{Bi}_2\text{Se}_3/\text{ZnO}$  heterostructures in comparison to the photoluminescence of the same thickness  
14  
15  
16 ZnO nanolayers deposited on p-doped Si substrates was observed. Correlation between the  
17  
18  
19 structure and optical properties of ZnO nanolayers in  $\text{Bi}_2\text{Se}_3/\text{ZnO}$  heterostructures is analyzed.  
20  
21  
22  
23  
24 Three complementary mechanisms of enhancement of optical properties of ZnO in  $\text{Bi}_2\text{Se}_3/\text{ZnO}$   
25  
26  
27 heterostructures, based on charge separation at the  $\text{Bi}_2\text{Se}_3/\text{ZnO}$  interface, improvement of ZnO  
28  
29  
30 crystalline structure and surface plasmon-photon coupling are proposed.  
31  
32  
33  
34  
35  
36  
37

## 38 INTRODUCTION

39  
40  
41

42 Zinc oxide (ZnO) is known as n-type semiconductor with good transparency and strong  
43  
44  
45 luminescence at room temperature.<sup>1</sup> The high photosensitivity, chemical stability and non-  
46  
47  
48 toxicity make it to be a promising material for applications in light emitting diodes (LEDs),<sup>2,3</sup>  
49  
50  
51 UV,<sup>4-9</sup> gas<sup>10</sup> and biosensors.<sup>11,12</sup>  
52  
53  
54  
55

1  
2  
3 Among different methods of fabrication, atomic layer deposition (ALD) provides homogenous  
4  
5  
6  
7 and conformal coating of ZnO on substrates with different shape and surface roughness.<sup>13–15</sup>  
8  
9  
10 Structure and optical properties of ZnO depend on type of substrate, temperature of deposition  
11  
12  
13 and thickness of the deposited layers.<sup>14–16</sup> It was shown that transition from amorphous to  
14  
15  
16  
17 crystalline structure in ZnO layers was observed with increasing of the layer thickness beyond  
18  
19  
20  
21 50 nm.<sup>14</sup> Improvement of ZnO crystalline structure in the layers with thicknesses below 50 nm  
22  
23  
24 was demonstrated in Al<sub>2</sub>O<sub>3</sub>/ZnO and graphene/ZnO nanolaminates, where ZnO layers were  
25  
26  
27  
28 deposited on Al<sub>2</sub>O<sub>3</sub> and graphene layers, respectively.<sup>15–18</sup> In addition to improvement of the  
29  
30  
31 crystalline structure, the optical properties of ZnO in the nanolaminate structures were found  
32  
33  
34  
35 to be dependent also on charge transfer on the interface between ZnO and Al<sub>2</sub>O<sub>3</sub>, and between  
36  
37  
38 ZnO and graphene.<sup>15–18</sup> Modelling of Al<sub>2</sub>O<sub>3</sub>/ZnO heterostructures confirmed that the  
39  
40  
41  
42 combination of ZnO (band gap ~3.3 eV) with a material with larger band gap as Al<sub>2</sub>O<sub>3</sub> (band  
43  
44  
45 gap ~ 6eV) results in increase of the photoluminescence (PL) of ZnO in Al<sub>2</sub>O<sub>3</sub>/ZnO  
46  
47  
48  
49 heterostructure due to the charge transfer at the interfaces and decrease of the surface  
50  
51  
52 potential in ZnO upper layers.<sup>16</sup> On the other hand, forming of heterostructures of ZnO and  
53  
54

1  
2  
3  
4 nanomaterials with the lower in comparison with ZnO band gap is advantageous for  
5  
6  
7 optoelectronic applications related to photoactive charge separation in visible and NIR range.  
8  
9

10  
11 Combination of nanolayers of ZnO and narrow band gap semiconductors as  $\text{Bi}_2\text{Se}_3$ ,  $\text{Bi}_2\text{Te}_3$   
12  
13  
14 or  $\text{Bi}_2\text{S}_3$  in heterostructures is a novel approach that can be implemented for optoelectronic  
15  
16  
17 devices and other applications. For instance,  $\text{Bi}_2\text{S}_3/\text{ZnO}$  heterostructures were recently  
18  
19  
20 demonstrated as an excellent photocatalyst for visible-light-driven hydrogen generation and a  
21  
22  
23 highly efficient photocatalyst for dye degradation under visible light irradiation.<sup>19</sup>  
24  
25  
26

27  
28 Bismuth selenide ( $\text{Bi}_2\text{Se}_3$ ) is a narrow band gap semiconductor, which belongs to a class of  
29  
30  
31 topological insulators with surface states protected from scattering by time reversal symmetry.<sup>20</sup>  
32  
33

34  
35 The presence of the surface states in  $\text{Bi}_2\text{Se}_3$  have been experimentally identified by reducing  
36  
37  
38 the bulk conductance using different approaches as tuning the gate voltage, introducing  
39  
40  
41 dopants and nanostructuring.<sup>21–23</sup>  
42  
43  
44

45  
46 Some previous research on optical, electronic properties of  $\text{ZnO}/\text{Bi}_2\text{Te}_3$  hybrid structures  
47  
48  
49 prepared by mechanical placement of exfoliated  $\text{Bi}_2\text{Te}_3$  flakes on the surface of ZnO crystal  
50  
51  
52 revealed enhancement of the PL of ZnO, which has been attributed to the surface plasmon  
53  
54

1  
2  
3 resonance.<sup>24</sup> It has been reported also that deposition of ZnO as protection nanolayer on top  
4  
5  
6  
7 of Bi<sub>2</sub>Se<sub>3</sub> nanostructures results in decrease of the free electron concentration in Bi<sub>2</sub>Se<sub>3</sub>.<sup>25</sup>  
8  
9  
10 However, the mechanisms of enhanced optical properties and correlation between optical and  
11  
12  
13 structural properties in such heterostructures have not been studied in detail.  
14  
15

16  
17 In this study, Bi<sub>2</sub>Se<sub>3</sub>/ZnO heterostructures were fabricated by ALD deposition of 10-150 nm  
18  
19  
20 thin ZnO nanolayers on top of Bi<sub>2</sub>Se<sub>3</sub> nanostructured coatings grown on graphene (further in  
21  
22  
23 text G/Bi<sub>2</sub>Se<sub>3</sub>/ZnO heterostructures) and quartz (further in text Q/Bi<sub>2</sub>Se<sub>3</sub>/ZnO heterostructures)  
24  
25  
26 by catalyst-free vapor-solid deposition.<sup>21,26</sup> Influence of Bi<sub>2</sub>Se<sub>3</sub> morphology on structure and on  
27  
28  
29 optical properties of ZnO nanolayers was investigated. The obtained results were compared  
30  
31  
32 with the properties of ZnO nanolayers deposited by ALD on p-doped Si substrates (further in  
33  
34  
35 text Si/ZnO heterostructures). Band gap diagram of the Bi<sub>2</sub>Se<sub>3</sub>/ZnO interface and possible  
36  
37  
38 mechanisms of PL enhancement in the Bi<sub>2</sub>Se<sub>3</sub>/ZnO heterostructures are discussed.  
39  
40  
41  
42  
43  
44  
45  
46

## 47 EXPERIMENTAL METHODS

48  
49  
50  
51  
52  
53  
54  
55

1  
2  
3 *Q/Bi<sub>2</sub>Se<sub>3</sub>/ZnO and G/Bi<sub>2</sub>Se<sub>3</sub>/ZnO heterostructure preparation.* Graphene substrates used for  
4  
5  
6  
7 the experiments were synthesized by copper-catalysed low-pressure chemical vapour  
8  
9  
10 deposition (CVD reactor First Nano Easy tube 101), using methane, diluted in hydrogen, as a  
11  
12  
13 carbon source. The synthesized graphene sheets were transferred onto quartz surface using  
14  
15  
16  
17 polymer-assisted transfer technique, as reported elsewhere.<sup>27,28</sup>  
18  
19  
20

21 Bi<sub>2</sub>Se<sub>3</sub> nanostructured coatings of thicknesses ~110 – 130 nm were synthesized using  
22  
23  
24 catalyst-free vapour-solid deposition method in a horizontal tube of single-zone quartz tube  
25  
26  
27  
28 furnace (GSL-1100X, MTI Corp.) on quartz and graphene substrates, as previously described  
29  
30  
31 elsewhere.<sup>26,29,30</sup> Bi<sub>2</sub>Se<sub>3</sub> crystals (99.99% Sigma Aldrich) were used as a source material, which  
32  
33  
34  
35 was evaporated at 585 °C temperature and deposited on substrates placed downstream at  
36  
37  
38  
39 330-380 °C temperature. The pressure inside the tube during the synthesis gradually increased  
40  
41  
42 from 200 mTorr to 4 Torr.  
43  
44

45 ZnO nanolayers of different thicknesses (from 10 nm to 150 nm) were synthesized onto  
46  
47  
48 prepared Bi<sub>2</sub>Se<sub>3</sub> nanostructures as well as on p-doped Si substrates ((100), Si-Mat) by ALD  
49  
50  
51  
52 method using a homemade reactor under the same conditions as described elsewhere.<sup>31</sup>  
53  
54  
55

1  
2  
3 Diethylzinc (95%, STREM Chemicals Inc.) was used as a zinc precursor and water – as an  
4  
5  
6  
7 oxidant. ZnO growth rate was 0.2 nm/cycle at 100 °C temperature.  
8  
9

10 *Characterisation.* The morphology and chemical composition of synthesized Q/Bi<sub>2</sub>Se<sub>3</sub>/ZnO  
11  
12  
13 and G/Bi<sub>2</sub>Se<sub>3</sub>/ZnO heterostructures were characterized using a field emission scanning  
14  
15  
16  
17 electron microscope (SEM) Hitachi S-4800 equipped with an energy dispersive X-ray (EDX)  
18  
19  
20  
21 analyser B-QANTAX.  
22  
23

24 The crystalline structure of fabricated heterostructures was studied using X-ray diffraction  
25  
26  
27 spectroscopy (XRD) by powder diffractometer X'PERT MRD with Cu K $\alpha$  radiation and high-  
28  
29  
30  
31 resolution transmission electron microscopy (HRTEM). For HRTEM characterization, an  
32  
33  
34  
35 electron transparent cross-section lamella was prepared by focused ion beam (FIB) milling and  
36  
37  
38  
39 lift-out in a Thermo Fisher Scientific Scios 2 Dual Beam SEM/FIB. The FIB lamella was attached  
40  
41  
42  
43 to a Cu half grid and further thinned by low keV milling using the Ga<sup>+</sup> beam. HRTEM was  
44  
45  
46  
47 performed on a FEI Titan environmental TEM with Image Cs corrector operating at 300 keV.  
48  
49  
50  
51  
52  
53  
54  
55  
56  
57  
58  
59  
60 Elemental analysis was carried out using a FEI Tecnai G2 F30 TEM equipped with an EDAX

1  
2  
3  
4 X-ray energy dispersive spectroscopy (XEDS) detector. Fast Fourier Transform (FFT) of the  
5  
6  
7 selected areas of the HRTEM images was performed using ImageJ software.  
8  
9

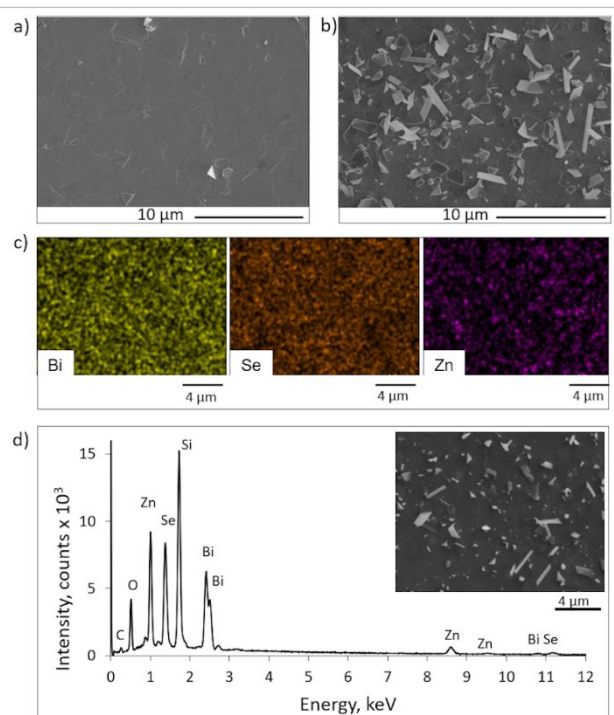
10 Optical properties of Q/Bi<sub>2</sub>Se<sub>3</sub>/ZnO and G/Bi<sub>2</sub>Se<sub>3</sub>/ZnO heterostructures were studied with UV-  
11  
12  
13  
14 Vis transmittance (fiber optics spectrometer Ocean Optics HR2000+), reflectance and PL  
15  
16  
17 spectroscopy in a wavelength range 340 - 775 nm. The excitation of luminescence was  
18  
19  
20 performed by a nitrogen laser source 266 nm wavelength (output 30 mW/cm<sup>2</sup>). The obtained  
21  
22  
23  
24 PL spectra were deconvoluted using MagicPlot 2.7.1.0 software by splitting the spectra in  
25  
26  
27  
28 separate peaks with the Gaussian fitting, keeping maxima positions of all subpeaks fixed within  
29  
30  
31  $\pm 0.02$  eV and full width at half maximum (FWHM) within  $\pm 0.03$  eV. The integrated PL intensity  
32  
33  
34  
35 was calculated from the values obtained after deconvolution by the multiplying the intensity of  
36  
37  
38 subpeak by its half width at half maximum (HWHM).  
39  
40  
41  
42  
43  
44

## 45 RESULTS AND DISCUSSION

46  
47  
48

49 *Morphology.* SEM images of G/Bi<sub>2</sub>Se<sub>3</sub> and Q/Bi<sub>2</sub>Se<sub>3</sub> nanostructured substrates covered with  
50  
51  
52 ZnO nanolayers show that the Bi<sub>2</sub>Se<sub>3</sub> coatings deposited on graphene surface consist from  
53  
54

1  
2  
3  
4 coalesced horizontally oriented nanoplates with rare inclusion of the nanoplates oriented under  
5  
6  
7 an angle relative to the substrate (Figure 1a). In contrast, in the  $\text{Bi}_2\text{Se}_3$  coatings deposited on  
8  
9  
10 quartz a significant number of randomly oriented nanoplates was observed (Figure 1b). The  
11  
12  
13  
14 EDX mapping showed that the ALD-deposited ZnO nanolayers uniformly covered the surface  
15  
16  
17 of  $\text{Bi}_2\text{Se}_3$  (Figure 1c).  
18  
19



20  
21  
22  
23  
24  
25  
26  
27  
28  
29  
30  
31  
32  
33  
34  
35  
36  
37  
38  
39  
40  
41  
42  
43  
44 **Figure 1.** SEM images of ~110-130 nm thin  $\text{Bi}_2\text{Se}_3$  nanostructures covered with 50 nm thin ZnO  
45  
46  
47 nanolayer: a) G/ $\text{Bi}_2\text{Se}_3$ /ZnO heterostructure, b) Q/ $\text{Bi}_2\text{Se}_3$ /ZnO heterostructure, c) an example  
48  
49  
50 of SEM-EDX mapping, and d) EDX spectrum of fabricated Q/ $\text{Bi}_2\text{Se}_3$ /ZnO heterostructure.  
51  
52  
53  
54  
55  
56  
57  
58  
59  
60

1  
2  
3  
4 The EDX measurements performed after the ZnO deposition (Figure 1d) showed that Bi and  
5  
6  
7 Se content in the fabricated G/Bi<sub>2</sub>Se<sub>3</sub>/ZnO and Q/Bi<sub>2</sub>Se<sub>3</sub>/ZnO heterostructures is respectively  
8  
9  
10 (39±3) at% and (61±3) at%, which within the measurement accuracy corresponds to the  
11  
12  
13 stoichiometric Bi<sub>2</sub>Se<sub>3</sub> compound. This confirms non-destructive nature of low-temperature (100  
14  
15  
16 °C) ALD ZnO deposition on already fabricated Bi<sub>2</sub>Se<sub>3</sub> nanostructures.  
17  
18  
19

20  
21 The XRD spectra of G/Bi<sub>2</sub>Se<sub>3</sub>/ZnO and Q/Bi<sub>2</sub>Se<sub>3</sub>/ZnO heterostructures revealed the  
22  
23  
24 crystalline nature of the deposited 10-100 nm thin ZnO nanolayers and underlying Bi<sub>2</sub>Se<sub>3</sub>  
25  
26  
27 (Figure 2). No reflections other than Bi<sub>2</sub>Se<sub>3</sub> compounds (for example Bi<sub>4</sub>Se<sub>3</sub>, Bi<sub>3</sub>Se<sub>4</sub>) or by-  
28  
29  
30 products that may form during ZnO ALD process on Bi<sub>2</sub>Se<sub>3</sub> (for example, ZnSe)<sup>32</sup> were  
31  
32  
33  
34  
35 detected.  
36  
37  
38  
39  
40  
41  
42  
43  
44  
45  
46  
47  
48  
49  
50  
51  
52  
53  
54  
55

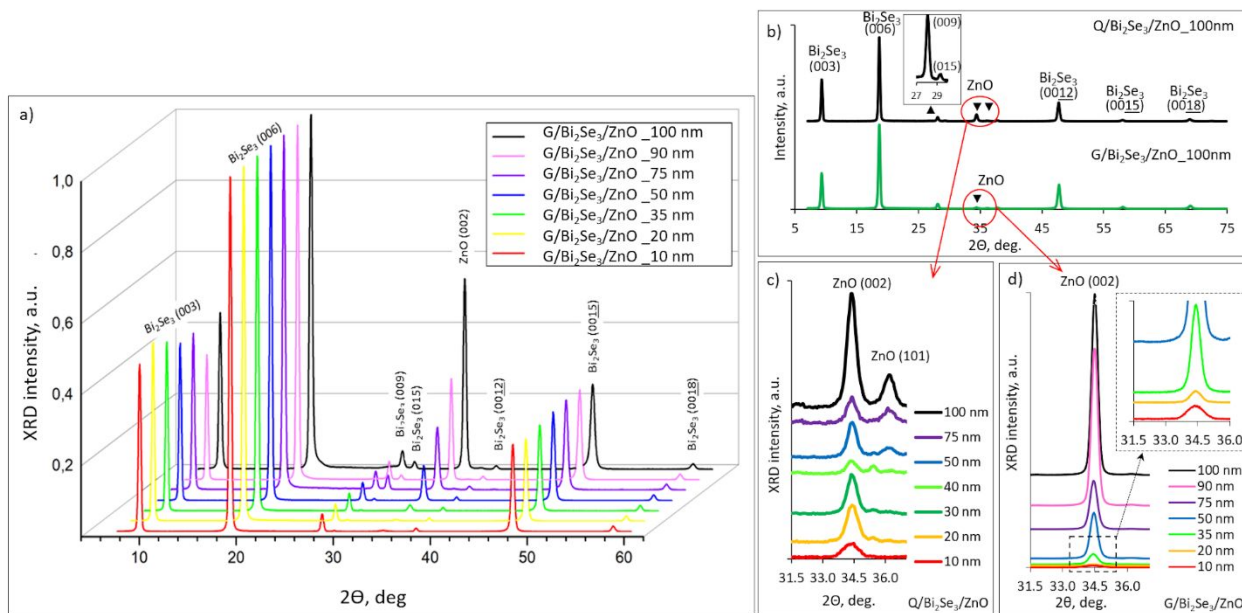


**Figure 2.** Full XRD spectra of a) G/Bi<sub>2</sub>Se<sub>3</sub>/ZnO heterostructures with ZnO nanolayers thicknesses 10-100 nm; b) G/Bi<sub>2</sub>Se<sub>3</sub>/ZnO (green) and Q/Bi<sub>2</sub>Se<sub>3</sub>/ZnO (black) heterostructures with ZnO nanolayer thickness 100 nm; c,d) enlarged images of the region of ZnO diffraction plane positions for the Q/Bi<sub>2</sub>Se<sub>3</sub>/ZnO (c) and G/Bi<sub>2</sub>Se<sub>3</sub>/ZnO (d and d, inset) heterostructures with different ZnO nanolayers thicknesses.

The highly intensive diffraction peaks at  $2\theta = 9.25^\circ$ ,  $18.57^\circ$ ,  $47.59^\circ$  and low intensity peaks at  $2\theta = 28.14^\circ$ ,  $37.86^\circ$  and  $58.18^\circ$  detected in XRD spectra of G/Bi<sub>2</sub>Se<sub>3</sub>/ZnO and Q/Bi<sub>2</sub>Se<sub>3</sub>/ZnO heterostructures (Figures 2a,b) correspond to (003), (006), (0015), (009), (0012) and (0018) reflection planes of rhombohedral crystal lattice of Bi<sub>2</sub>Se<sub>3</sub>.<sup>33</sup> This indicates the [00] growth

1  
2  
3 direction of synthesized by catalyst-free vapour-solid deposition method  $\text{Bi}_2\text{Se}_3$ , with the  
4  
5  
6  
7 crystallographic  $c$ -axis oriented perpendicularly to the substrate surface. XRD of Q/ $\text{Bi}_2\text{Se}_3$ /ZnO  
8  
9  
10 heterostructures revealed also low intensity peak at  $2\theta = 29.36^\circ$ , indicating (015) reflection  
11  
12  
13 plane of  $\text{Bi}_2\text{Se}_3$  (Figure 2b black line, inset). This diffraction peak can be attributed to the  
14  
15  
16 presented in the Q/ $\text{Bi}_2\text{Se}_3$ /ZnO heterostructures  $\text{Bi}_2\text{Se}_3$  nanoplates oriented under different  
17  
18  
19 angles relative to the substrate surface (Figure 1b).<sup>26</sup>  
20  
21  
22  
23

24 The XRD spectra obtained for the fabricated G/ $\text{Bi}_2\text{Se}_3$ /ZnO and Q/ $\text{Bi}_2\text{Se}_3$ /ZnO  
25  
26  
27 heterostructures (Figures 2a,b) were used for the study of the absence or presence of  
28  
29  
30 characteristic for ZnO diffraction peaks and for the extraction of their FWHM values.  
31  
32  
33

34 The ZnO lattice constant  $c$  and  $d$ -spacing between the atomic planes for ZnO nanolayers  
35  
36  
37 were calculated from the obtained XRD spectra of Q/ $\text{Bi}_2\text{Se}_3$ /ZnO and G/ $\text{Bi}_2\text{Se}_3$ /ZnO  
38  
39  
40 heterostructures, applying formula for hexagonal ZnO crystal lattice:<sup>34</sup>  
41  
42  
43

$$\frac{1}{d^2} = \frac{4}{3} \cdot \left( \frac{h^2 + kh + k^2}{a^2} \right) + \frac{l^2}{c^2}$$

44  
45  
46  
47  
48  
49  
50 (1)

51  
52  
53 where  $d$  is interplanar spacing;  $h, k, l$  are Miller indices;  $a$  and  $c$  are lattice constants.  
54  
55

1  
2  
3  
4 The calculated values for ZnO lattice constant  $c$  and d-spacing were  $(0.521 \pm 0.014)$  nm and  
5  
6  
7  $(0.261 \pm 0.005)$  nm respectively for ZnO nanolayers in both G/Bi<sub>2</sub>Se<sub>3</sub>/ZnO and Q/Bi<sub>2</sub>Se<sub>3</sub>/ZnO  
8  
9  
10 heterostructures. These values are consistent with the ZnO lattice parameters for 100 nm ALD  
11  
12  
13 thin film deposited on Si substrate (( $c = 0.5213$  nm and  $d = 0.2606$  nm)<sup>14</sup>.  
14  
15  
16

17 Presence of characteristic for ZnO diffraction peaks already for 10 nm thick ZnO layers  
18  
19  
20 indicates highly crystalline structure of 10-100 nm thin ZnO nanolayers in G/Bi<sub>2</sub>Se<sub>3</sub>/ZnO and  
21  
22  
23 Q/Bi<sub>2</sub>Se<sub>3</sub>/ZnO heterostructures in comparison with Si/ZnO heterostructures, where the  
24  
25  
26 transition from amorphous (below 20 nm of thickness) and semi-amorphous (of thicknesses 20-  
27  
28  
29 50 nm) to crystalline state was observed for ZnO thicknesses starting from 50 nm.<sup>31</sup>  
30  
31  
32  
33

34 For all G/Bi<sub>2</sub>Se<sub>3</sub>/ZnO heterostructures, the only detected ZnO reflection peak corresponds to  
35  
36  
37 (002) plane (Figure 2d, peak at  $2\theta=34.38^\circ$ ). This indicates one-direction growth of ZnO grains  
38  
39  
40 on G/Bi<sub>2</sub>Se<sub>3</sub> substrate and differs significantly from the ALD growth of ZnO on Si, which results  
41  
42  
43 in formation of polycrystalline thin films, showing two main diffractions peaks corresponding to  
44  
45  
46 (100) and (101) reflection planes.<sup>31</sup>  
47  
48  
49  
50  
51  
52  
53  
54  
55

1  
2  
3 For the Q/Bi<sub>2</sub>Se<sub>3</sub>/ZnO heterostructures, the reflection peak of ZnO (002) plane was also  
4  
5  
6  
7 dominating for all range of ZnO thicknesses, however, its intensity was lower in comparison  
8  
9  
10 with G/Bi<sub>2</sub>Se<sub>3</sub>/ZnO samples. One of two characteristic for polycrystalline ALD-deposited on Si  
11  
12  
13 substrates ZnO films diffraction peaks – the peak related to (101) reflection plane - was detected  
14  
15  
16 for Q/Bi<sub>2</sub>Se<sub>3</sub>/ZnO samples with ZnO thicknesses starting from 50 nm (Figure 2c). Therefore, in  
17  
18  
19 contrast with the G/Bi<sub>2</sub>Se<sub>3</sub>/ZnO heterostructures, promoting one-direction growth of ZnO grains,  
20  
21  
22 the Q/Bi<sub>2</sub>Se<sub>3</sub> substrates promote also growth of ZnO grains in one of directions, characteristic  
23  
24  
25 also for Si/ZnO thin films, starting from the ZnO nanolayers thicknesses of 50 nm. However,  
26  
27  
28 the absence of the main for Si/ZnO thin films (100) diffraction peak in Q/Bi<sub>2</sub>Se<sub>3</sub>/ZnO XRD  
29  
30  
31 spectra indicates ZnO growth mechanism like G/Bi<sub>2</sub>Se<sub>3</sub>/ZnO heterostructures. The lower in  
32  
33  
34 comparison with G/Bi<sub>2</sub>Se<sub>3</sub>/ZnO heterostructures intensities of the ZnO (002) reflection peak and  
35  
36  
37 the presence of the (101) reflection peak may be explained by the morphology of the Q/Bi<sub>2</sub>Se<sub>3</sub>  
38  
39  
40 substrate surface, promoting growth of the ZnO nanolayers not only parallel to the quartz  
41  
42  
43 surface, but also under different directions relative to it (on surfaces of the randomly oriented  
44  
45  
46 Bi<sub>2</sub>Se<sub>3</sub> nanoplates).  
47  
48  
49  
50  
51  
52  
53  
54  
55  
56  
57  
58  
59  
60

Figure 3a confirms the orientation of ZnO crystalline grains in different directions in the Q/Bi<sub>2</sub>Se<sub>3</sub>/ZnO heterostructure with ZnO nanolayer thickness 50 nm.

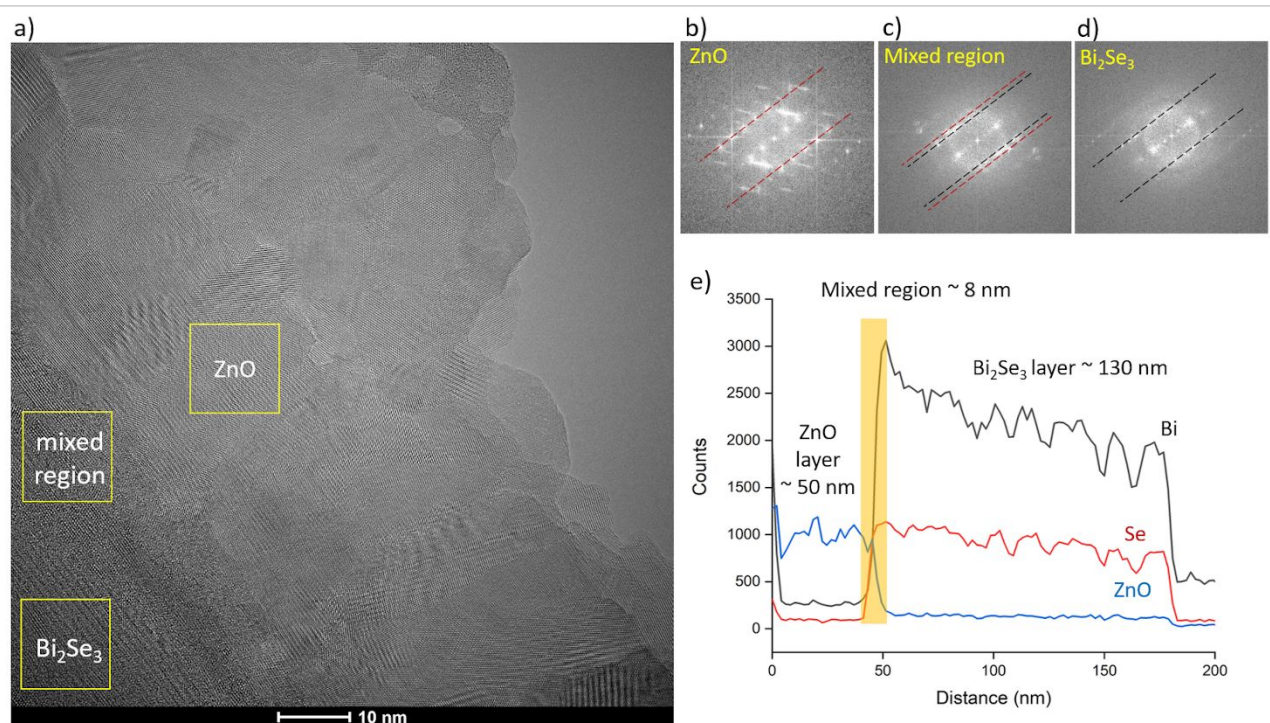


Figure 3. a) HRTEM image of the crosssection of Q/Bi<sub>2</sub>Se<sub>3</sub>/ZnO heterostructure with ZnO nanolayer thickness 50 nm; b-d) FFT images of ZnO, mixed region at the Bi<sub>2</sub>Se<sub>3</sub>/ZnO interface and Bi<sub>2</sub>Se<sub>3</sub>, taken from the areas of the sample labelled with squares at the HRTEM image; e) Line EDX scan of the crosssection of the Q/Bi<sub>2</sub>Se<sub>3</sub>/ZnO (50 nm) sample.

FFT and XEDS analysis performed for the crosssection of Q/Bi<sub>2</sub>Se<sub>3</sub>/ZnO heterostructure (Figures 3b-e) revealed the presence of approximately 8 nm thin transition layer at the

1  
2  
3  
4 Bi<sub>2</sub>Se<sub>3</sub>/ZnO interface. Beyond this thickness, the ZnO nanolayer was found to be consisting of  
5  
6  
7 crystalline grains (Figure 3a).  
8  
9

10 The apparent crystalline grain sizes were estimated from the ZnO (002) diffraction peaks of  
11  
12  
13 the XRD spectra of G/Bi<sub>2</sub>Se<sub>3</sub>/ZnO and Q/Bi<sub>2</sub>Se<sub>3</sub>/ZnO heterostructures using the Scherrer's  
14  
15  
16  
17 equation<sup>35</sup>:  
18  
19

$$D = \frac{K \cdot \lambda}{\beta \cdot \cos(\theta)}$$

20  
21  
22  
23  
24  
25 (2)  
26  
27

28 where  $\lambda$  is the X-ray wavelength,  $\beta$  is the integral half width,  $\theta$  is the Bragg angle. K factor  
29  
30  
31 value in this study equals 0.9 for considering not spherical shapes of the ZnO crystalline grains  
32  
33  
34  
35 confirmed by the HRTEM images (Figures 3a,4a).  
36  
37

38 The lattice strain  $\varepsilon$  in ZnO was calculated using the following formula:<sup>35</sup>  
39  
40

$$\varepsilon = \frac{\beta}{4 \tan(\theta)}$$

41  
42  
43  
44  
45  
46 (3)  
47  
48  
49

50 For more accurate analysis of grain size and strain effects, the instrumental line broadening  
51  
52  
53 must be accounted. The instrumental corrected broadening was calculated as follows:<sup>35</sup>  
54  
55

$$\beta = [(\beta_{\text{measured}})^2 - (\beta_{\text{instrumental}})^2]^{1/2} \quad (4)$$

It should be noted that even accounting the instrumental broadening, the precision of the grain size determination may be  $\pm 10\text{-}15\%$ . Thus, in what follows, the general tendencies of the changes in grain sizes, not calculation of the exact ZnO grain sizes, are considered. The apparent crystalline grain size and lattice strain values for ZnO nanolayers, estimated using Equations (2) - (4) respectively, are shown in Figure 4 b,c.

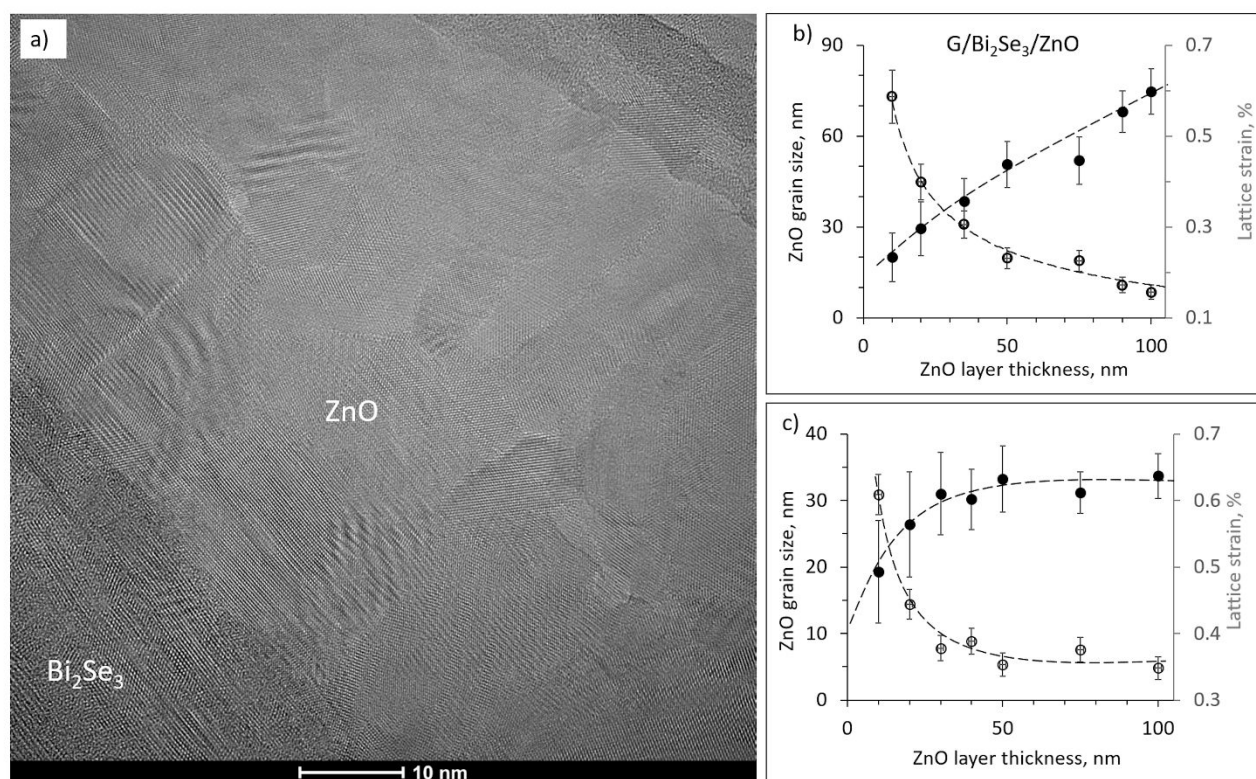


**Figure 4.** a) HRTEM image of the crosssection of Q/Bi<sub>2</sub>Se<sub>3</sub>/ZnO heterostructure (thickness of ZnO nanolayer 50 nm); b-c) Apparent ZnO grain size (primary y-axis, black circles) and lattice

1  
2  
3 strain (secondary y-axis, hollow circles) vs ZnO nanolayers thickness in b) G/Bi<sub>2</sub>Se<sub>3</sub>/ZnO, and  
4  
5  
6  
7 c) Q/Bi<sub>2</sub>Se<sub>3</sub>/ZnO heterostructures.  
8  
9

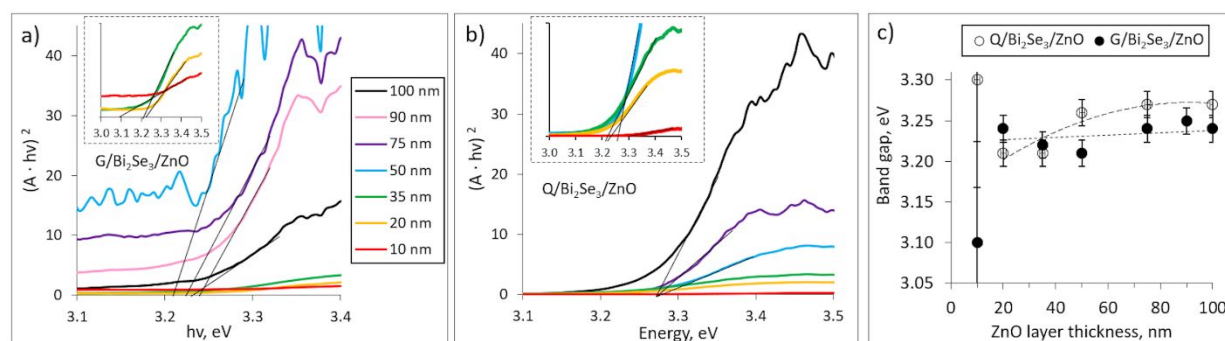
10  
11 G/Bi<sub>2</sub>Se<sub>3</sub>/ZnO heterostructures (Figure 4b) showed nearly linear tendency of increase of  
12  
13  
14 apparent grain size with the increase of ZnO nanolayer thickness, reaching values of approx.  
15  
16  
17  
18 75 nm for the 100 nm thin ZnO nanolayers, accompanied by simultaneous decrease of the  
19  
20  
21  
22 lattice strain from 0.6% down to 0.15%. This indicates the improvement of the ZnO crystalline  
23  
24  
25 structure with the increase of ZnO nanolayer thickness. In contrast, for Q/Bi<sub>2</sub>Se<sub>3</sub>/ZnO  
26  
27  
28 heterostructures an increase in grain size, accompanied by a decrease in the lattice stress, was  
29  
30  
31  
32 observed only for ZnO nanolayer thicknesses below 30 nm (Figure 4c). Above this value, the  
33  
34  
35  
36 average ZnO grain size in the Q/Bi<sub>2</sub>Se<sub>3</sub>/ZnO heterostructures is approximately 30 nm and is  
37  
38  
39 practically unchanged, which is consistent with the sizes of grains visible at the HRTEM image  
40  
41  
42 (Figure 4a). The smaller average size of the ZnO grains is probably related to the surface  
43  
44  
45 morphology of the Q/Bi<sub>2</sub>Se<sub>3</sub> substrates, when ZnO growing on Bi<sub>2</sub>Se<sub>3</sub> nanoplates of different  
46  
47  
48 orientations start to interfere with each other, thus hampering the formation of larger grains.  
49  
50  
51  
52  
53 Such difference between the grain sizes in G/Bi<sub>2</sub>Se<sub>3</sub>/ZnO and Q/Bi<sub>2</sub>Se<sub>3</sub>/ZnO heterostructures  
54  
55

may lead to a higher number of formed at the ZnO grain boundaries optically active defects in Q/Bi<sub>2</sub>Se<sub>3</sub>/ZnO heterostructures in comparison with G/Bi<sub>2</sub>Se<sub>3</sub>/ZnO heterostructures.

**Optical properties.** Optical band gap ( $E_g$ ) values for the ZnO nanolayers of G/Bi<sub>2</sub>Se<sub>3</sub>/ZnO and Q/Bi<sub>2</sub>Se<sub>3</sub>/ZnO heterostructures were estimated assuming a direct transition between valence and conduction bands and using the Tauc equation :<sup>14</sup>

$$ah\nu = B(h\nu - E_g)^r \quad (5)$$

where B is the constant,  $a$  is the absorption coefficient,  $h\nu$  is the incident photon energy, and  $r$  is the constant, which for direct transition equals  $\frac{1}{2}$ .<sup>36</sup>  $E_g$  was graphically determined from the Tauc plots of  $(ah\nu)^2$  vs  $h\nu$  (Figures 5a and 5b) by extrapolation the linear part of the absorption edge to  $ah\nu = 0$ .



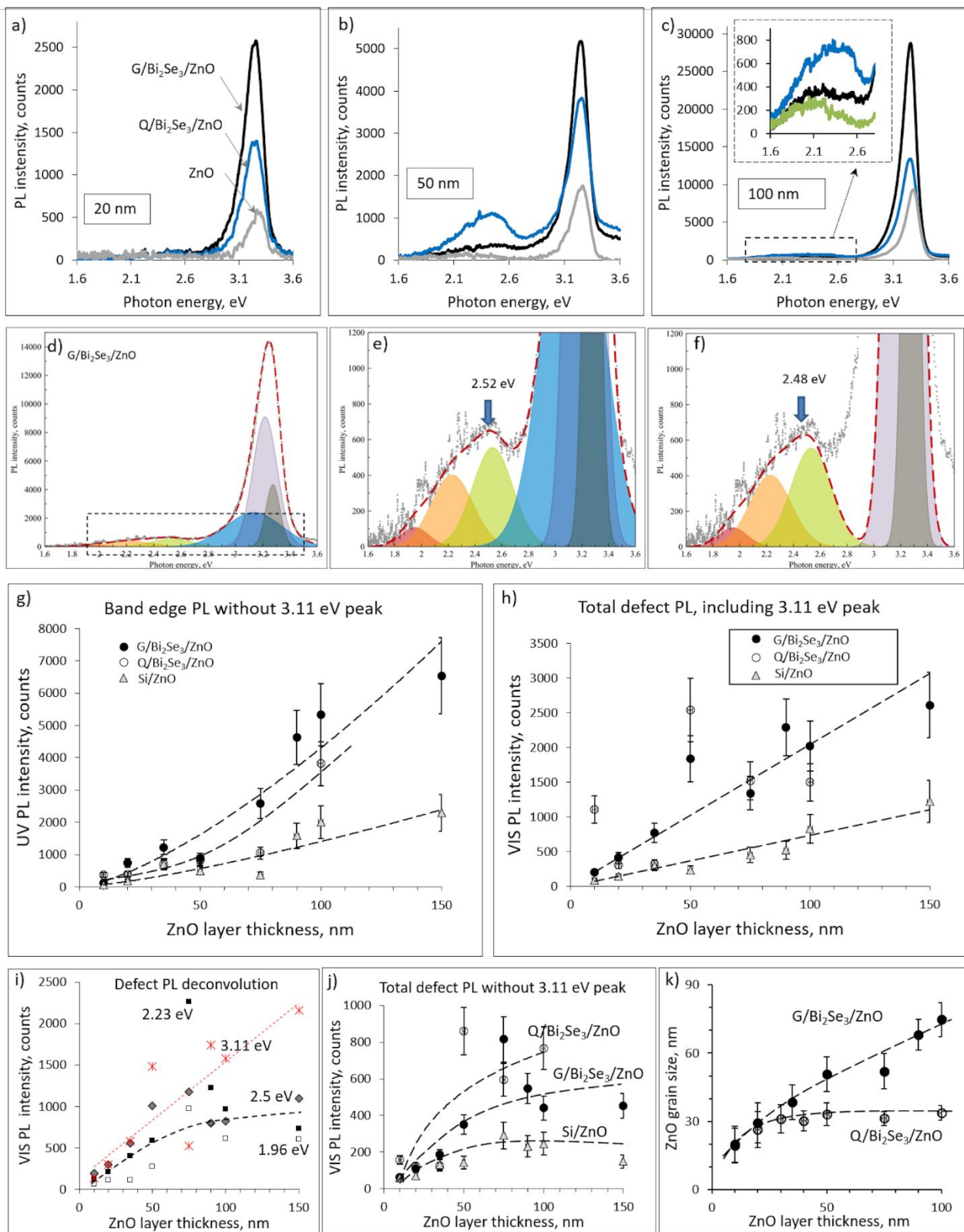
1  
2  
3 **Figure 5.** Band gap determination on the absorption edge from absorbance spectra for the ZnO  
4  
5  
6  
7 nanolayers of different thicknesses in (a) G/Bi<sub>2</sub>Se<sub>3</sub>/ZnO and (b) Q/Bi<sub>2</sub>Se<sub>3</sub>/ZnO heterostructures;  
8  
9  
10  
11 c) Band gap values vs ZnO nanolayer thickness in Q/Bi<sub>2</sub>Se<sub>3</sub>/ZnO and G/Bi<sub>2</sub>Se<sub>3</sub>/ZnO  
12  
13  
14 heterostructures.  
15  
16  
17

18 The determined from the absorption spectra band gap values of ZnO nanolayers varied from  
19  
20  
21 3.21 to 3.27 eV and from 3.21 to 3.25 eV for in Q/Bi<sub>2</sub>Se<sub>3</sub>/ZnO and G/Bi<sub>2</sub>Se<sub>3</sub>/ZnO  
22  
23  
24 heterostructures respectively (Figure 5 c). It should be noted that band gaps for 10 nm ZnO  
25  
26  
27  
28  
29 nanolayers are not taken into account in this data analysis as were determined with low  
30  
31  
32 accuracy. The weak absorption signal detected (insets of Figures 5a and 5b) may be related  
33  
34  
35  
36 by the presence of the observed in HRTEM images 8 nm thin transition layer at the Bi<sub>2</sub>Se<sub>3</sub>/ZnO  
37  
38  
39 interface (Figure 3).  
40  
41  
42

43 The obtained band gap values of ZnO in G/Bi<sub>2</sub>Se<sub>3</sub>/ZnO and Q/Bi<sub>2</sub>Se<sub>3</sub>/ZnO heterostructures  
44  
45  
46 were consistent with the optical band gap values reported previously for ZnO thin films on Si  
47  
48  
49 substrates (3.2 eV)<sup>31,36</sup> and are lower than typical band gap value of ZnO single crystal (3.37  
50  
51  
52  
53 eV).<sup>37</sup> Such optical band gap redshift of the ZnO nanolayers in Bi<sub>2</sub>Se<sub>3</sub>/ZnO heterostructures in  
54  
55

1  
2  
3 comparison with the bulk ZnO may be related to higher (in comparison with single ZnO crystal)  
4  
5  
6 number of optically active point defects like Zn, O vacancies and Zn interstitials formed in the  
7  
8 ZnO nanolayer near the Bi<sub>2</sub>Se<sub>3</sub>/ZnO interface, as well as at the ZnO grain boundaries. These  
9  
10 defects may form shallow states in close to the conduction and valence bands of ZnO.<sup>14,31,38–40</sup>  
11  
12  
13  
14  
15  
16  
17 In this case, zone-to-centre transitions would result in reduction of the band gap value  
18  
19  
20  
21 comparing to bulk ZnO.  
22  
23

24 ***Photoluminescence*** (PL) of the ZnO nanolayers in Q/Bi<sub>2</sub>Se<sub>3</sub>/ZnO and G/Bi<sub>2</sub>Se<sub>3</sub>/ZnO  
25  
26  
27 heterostructures was compared to the PL of the same thickness ALD ZnO thin films in Si/ZnO  
28  
29  
30  
31 heterostructures. Generally, the PL spectra of all types of ZnO nanolayers exhibited two  
32  
33  
34  
35 maxima (Figures 6 a-c): an intensive peak at ~3.2 eV and a broad peak centred at 2.3-2.4 eV.  
36  
37  
38  
39  
40  
41  
42  
43  
44  
45  
46  
47  
48  
49  
50  
51  
52  
53  
54



1  
2  
3 **Figure 6.** Photoluminescence spectra of Q/Bi<sub>2</sub>Se<sub>3</sub>/ZnO, G/Bi<sub>2</sub>Se<sub>3</sub>/ZnO heterostructures and for  
4  
5  
6  
7 the comparison - of ZnO thin films with different ZnO nanolayer thicknesses: a) 20 nm, b) 50  
8  
9  
10 nm, c) 100 nm; d) an example of deconvoluted G/Bi<sub>2</sub>Se<sub>3</sub>/ZnO spectrum; e) deconvolution of the  
11  
12  
13  
14 defect emission peak; f) deconvolution of the defect emission peak without the contribution of  
15  
16  
17 the defect peak related to the neutral Zn vacancies; g) band edge PL intensities of the  
18  
19  
20 G/Bi<sub>2</sub>Se<sub>3</sub>/ZnO, Q/Bi<sub>2</sub>Se<sub>3</sub>/ZnO and Si/ZnO vs ZnO nanolayer thickness; h) defect ZnO emission  
21  
22  
23  
24 intensities of the G/Bi<sub>2</sub>Se<sub>3</sub>/ZnO, Q/Bi<sub>2</sub>Se<sub>3</sub>/ZnO and Si/ZnO vs ZnO nanolayer thickness (with  
25  
26  
27 the contribution of 3.11 eV peak related to the neutral Zn vacancies); i) intensities of emission  
28  
29  
30  
31 peaks related to different types of defects thickness for G/Bi<sub>2</sub>Se<sub>3</sub>/ZnO heterostructures vs ZnO  
32  
33  
34  
35 nanolayer thickness; j) defect ZnO emission intensities (without the contribution of 3.11 eV peak  
36  
37  
38 related to the neutral Zn vacancies) of the G/Bi<sub>2</sub>Se<sub>3</sub>/ZnO, Q/Bi<sub>2</sub>Se<sub>3</sub>/ZnO and Si/ZnO vs ZnO  
39  
40  
41  
42 nanolayer thickness and k) comparison between the ZnO grain sizes in G/Bi<sub>2</sub>Se<sub>3</sub>/ZnO and  
43  
44  
45 Q/Bi<sub>2</sub>Se<sub>3</sub>/ZnO vs ZnO thickness.

46  
47  
48  
49 Deconvolution of the photoluminescence spectra performed by Gaussian fitting (Figures 6d  
50  
51  
52 and 6e) revealed the presence of two PL peaks centered at 3.24 and 3.3 eV, which can be  
53  
54  
55

1  
2  
3 related to the ZnO band edge emission, and four PL peaks that can be related to the charge  
4  
5  
6  
7 carrier recombination on different types of defects, such as neutral zinc interstitials (peak  
8  
9  
10 centred at  $\sim 3.11$  eV), singly ionized oxygen and zinc vacancies (peak centred at  $\sim 2.5$  eV),  
11  
12  
13  
14 double ionized oxygen vacancies (peak centred at  $\sim 2.23$  eV) and oxygen interstitials (peak  
15  
16  
17 centred at  $\sim 1.96$  eV).<sup>31,41,42</sup>  
18  
19  
20

21 As it can be seen from Figure 6e, the emission peak related to the neutral zinc interstitials  
22  
23  
24 ( $\sim 3.11$  eV) is significantly contributing to the total intensities of both maxima of the PL spectra.  
25  
26  
27 Traditionally, the influence of this peak is not separated from the summarized intensities of the  
28  
29  
30 band-edge and visible defect PL peaks of ZnO. In this work, the contribution of the defect  
31  
32  
33  
34 emission peak centred at  $\sim 3.11$  eV is removed from the total intensities of the band-edge and  
35  
36  
37  
38 visible defect PL peaks as illustrated in Figure 6f in order to analyse the dynamics of the band-  
39  
40  
41 edge PL peaks centred at 3.24 eV and 3.3 eV, and the defect PL peaks centred at 1.96 eV,  
42  
43  
44  
45 2.23 eV and 2.5 eV.  
46  
47  
48

49 ***Band-edge ZnO photoluminescence (3.24 eV, 3.3 eV).*** The intensity of the band-edge PL of  
50  
51  
52 ZnO in G/Bi<sub>2</sub>Se<sub>3</sub>/ZnO and Q/Bi<sub>2</sub>Se<sub>3</sub>/ZnO heterostructures for all ZnO nanolayer thicknesses  
53  
54

was found to be significantly enhanced (by factor  $\sim 3.3$  and  $\sim 1.7$  respectively) in comparison with Si/ZnO heterostructures (Figure 6g). Enhancement of the band-edge PL of ZnO may be a result of superposition of several mechanisms: (i) charge transfer between the  $\text{Bi}_2\text{Se}_3$  and ZnO nanolayers, (ii) improvement of crystalline structure of ZnO during the growth, and (iii) coupling of the band-edge excitons to surface-plasmon polaritons.

Charge transfer at the  $\text{Bi}_2\text{Se}_3/\text{ZnO}$  interface can be analysed within a band diagram (Figure 7a).

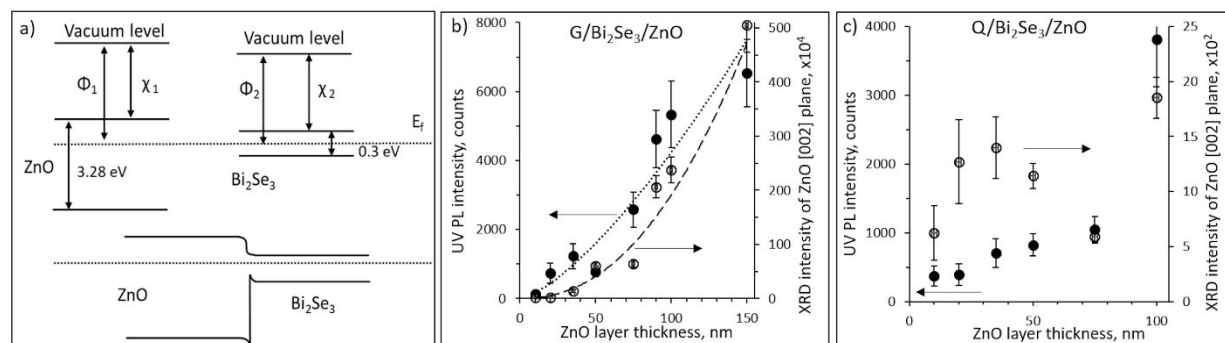


**Figure 7.** a) Band diagram for the  $\text{Bi}_2\text{Se}_3/\text{ZnO}$  interface. b,c) Dependence of ZnO PL intensity (primary y axis, black circles, dotted line) and XRD peak intensity (secondary y axis, hollow circles, dashed line) of G/ $\text{Bi}_2\text{Se}_3/\text{ZnO}$  (b) and Q/ $\text{Bi}_2\text{Se}_3/\text{ZnO}$  (c) heterostructures.

1  
2  
3  
4 After forming a heterostructure, alignment of the Fermi level ( $E_f$ ) in both contacting materials  
5  
6  
7 will occur. Position of the Fermi level  $E_F$  in each component of the heterostructure before joining  
8  
9  
10 them together was estimated as follows:<sup>16</sup>

$$11 \quad E_F = \Phi - \chi, \quad (6)$$

12  
13  
14 where  $\Phi$  is the work function and  $\chi$  is the electron affinity.

15  
16  
17 The conductance band and valence band gap offsets were calculated as

$$18 \quad \Delta E_c = \chi_2 - \chi_1 \quad (7)$$

$$19 \quad \Delta E_v = \Delta E_g - \Delta E_c \quad (8)$$

20  
21 where  $\Delta E_g$  is the difference between the band gap values of ZnO and Bi<sub>2</sub>Se<sub>3</sub>, and  $\chi_1$  and  $\chi_2$   
22  
23  
24 are the electron affinities of ZnO and Bi<sub>2</sub>Se<sub>3</sub> respectively.

25  
26  
27 The built-in potential  $V_{bi}$  between the two altering ZnO and Bi<sub>2</sub>Se<sub>3</sub> nanolayers was calculated  
28  
29  
30 as

$$31 \quad V_{bi} \cdot q = E_{F1} - E_{F2} \quad (9)$$

32  
33  
34 where  $q$  is the electron charge,  $E_{F1}$  and  $E_{F2}$  are Fermi level positions in ZnO and Bi<sub>2</sub>Se<sub>3</sub>,  
35  
36  
37 correspondently.

Values of  $\text{Bi}_2\text{Se}_3$  and ZnO parameters (work function, electron affinity and band gap), shown in Table 1 were taken from literature due to restriction of X-ray and ultraviolet photoelectron spectroscopy (XPS/UPS) methods for thick layers (over 20 nm).<sup>16,43–45</sup> The estimated by Equations (6)-(9) offsets of conductance band and valence  $\Delta E_c$ ,  $\Delta E_v$ , and built in potential  $V_{bi}$ , between  $\text{Bi}_2\text{Se}_3$  and ZnO are summarized in Table 1.

Table 1. Electronic parameters of ZnO and  $\text{Bi}_2\text{Se}_3$ .

	$\Phi$ , eV	$X$ , eV	$E_g$ , eV	$\Delta E_c$ , eV	$\Delta E_v$ , eV	$V_{bi}$ , eV
ZnO <sup>16</sup>	5.8	4.35	3.28	0.95	2.03	1.35
$\text{Bi}_2\text{Se}_3$ <sup>43–46</sup>	5.4	5.3	0.3			

In contrast with Si/ZnO deposited on p-doped Si substrates, where the depleted regions are formed near the interface in both Si and ZnO, the junction of ZnO and  $\text{Bi}_2\text{Se}_3$  in a heterostructure results in formation of the electron-rich and hole-rich areas in ZnO and  $\text{Bi}_2\text{Se}_3$ , respectively. Forming of the hole-rich region in  $\text{Bi}_2\text{Se}_3$  will result in decrease of electron concentration in this material.<sup>25</sup> Forming of the electron-rich area in ZnO will reduce the depletion layer formed at the surface of ZnO due to the chemisorption of oxygen.<sup>14,16,46</sup> This depletion layer separates electrons and holes created by the above-bandgap illumination and

1  
2  
3 restricts the exciton formation. Reduction of the depletion layer of ZnO due to formation of the  
4  
5  
6  
7  $\text{Bi}_2\text{Se}_3/\text{ZnO}$  heterojunction will lead to an increase of the band-edge PL of ZnO in comparison  
8  
9  
10 with the ZnO of the same thickness, deposited on p-doped Si substrates.  
11  
12  
13

14 However, the equal for both G/ $\text{Bi}_2\text{Se}_3/\text{ZnO}$  and Q/ $\text{Bi}_2\text{Se}_3/\text{ZnO}$  heterostructures decrease of  
15  
16  
17 the ZnO depletion layer does not explain the significantly higher band-edge PL of the ZnO in  
18  
19  
20 G/ $\text{Bi}_2\text{Se}_3/\text{ZnO}$  heterostructures in comparison with the band-edge PL of the ZnO in  
21  
22  
23 Q/ $\text{Bi}_2\text{Se}_3/\text{ZnO}$  heterostructures (Figure 6g). This difference may be the result of other  
24  
25  
26  
27 mechanisms of PL enhancement, discussed in the following paragraphs.  
28  
29  
30

31 Figures 7b and 7c illustrate the correlation between the intensity of the XRD peak related to  
32  
33  
34 the ZnO (002) reflection plane and the intensity of the band-edge PL emission of ZnO in  
35  
36  
37  
38  $\text{Bi}_2\text{Se}_3/\text{ZnO}$  heterostructures.  
39  
40

41  
42 The increase of the intensities of the XRD and the band-edge PL peaks with the increase of  
43  
44  
45 the ZnO thickness for the ZnO nanolayers in G/ $\text{Bi}_2\text{Se}_3/\text{ZnO}$  heterostructures (Figure 7a) is in  
46  
47  
48  
49 line with the data related to the ZnO grain sizes (Figure 6k) and proves the role of improvement  
50  
51  
52 of the crystalline structure of the ZnO as one of the mechanisms for the band-edge PL  
53  
54  
55

1  
2  
3 enhancement. For the ZnO nanolayers in Q/Bi<sub>2</sub>Se<sub>3</sub>/ZnO heterostructures, the correlation  
4  
5  
6  
7 between the values of intensities of XRD and band-edge PL is not convincing (Figure 7c),  
8  
9  
10 however, both PL and XRD intensities tend to increase at ZnO thickness above 75 nm.  
11  
12  
13 Presumably, in this case the ZnO crystallinity improvement is not the dominating mechanism  
14  
15  
16 for the band-edge PL enhancement. This conclusion is supported by the data shown in Figure  
17  
18  
19  
20  
21 6k, demonstrating no increase of the ZnO grain size in Q/Bi<sub>2</sub>Se<sub>3</sub>/ZnO with the increase of the  
22  
23  
24 thickness of ZnO nanolayer.  
25  
26  
27

28 However, the larger increase of the ZnO PL in the heterostructures in comparison with the  
29  
30  
31 increase of the intensity of the XRD peak (Figures 7b and 7c) may indicate the influence of the  
32  
33  
34 third mechanism of the PL enhancement, which is the coupling of the band-edge excitons to  
35  
36  
37 Bi<sub>2</sub>Se<sub>3</sub> surface-plasmon polaritons similarly to the PL enhancement reported for the  
38  
39  
40 mechanically prepared ZnO/Bi<sub>2</sub>Te<sub>3</sub> heterostructures.<sup>24</sup>  
41  
42  
43  
44

45 ***ZnO defect photoluminescence.*** The data on intensities of four peaks of ZnO defect emission  
46  
47  
48 related to different types of defects (neutral zinc interstitials (~3.11 eV), singly ionized oxygen  
49  
50  
51 and zinc vacancies (~2.5 eV), double ionized oxygen vacancies (~2.23 eV) and oxygen  
52  
53  
54

1  
2  
3 interstitials ( $\sim 1.96$  eV)) for G/Bi<sub>2</sub>Se<sub>3</sub>/ZnO, Q/Bi<sub>2</sub>Se<sub>3</sub>/ZnO and Si/ZnO are summarized in Figure  
4  
5  
6  
7 6 h. The defect PL of the ZnO nanolayers in G/Bi<sub>2</sub>Se<sub>3</sub>/ZnO heterostructures was 1.5-3 times  
8  
9  
10 higher in comparison with Si/ZnO heterostructures and showed linear increase with the ZnO  
11  
12  
13 nanolayer thickness. For the ZnO nanolayers in Q/Bi<sub>2</sub>Se<sub>3</sub>/ZnO heterostructures, the defect PL  
14  
15  
16 for different ZnO nanolayers thicknesses was up to 6 times higher in comparison with the defect  
17  
18  
19 PL of the Si/ZnO. The significantly higher defect PL of ZnO in Q/Bi<sub>2</sub>Se<sub>3</sub>/ZnO heterostructures  
20  
21  
22 in comparison with G/Bi<sub>2</sub>Se<sub>3</sub>/ZnO heterostructures may be explained by the smaller ZnO grain  
23  
24  
25 sizes resulting in larger area of grain boundaries in Q/Bi<sub>2</sub>Se<sub>3</sub>/ZnO heterostructures. The scatter  
26  
27  
28 of the intensity values in this case (Figure 6h, hollow circles) is presumably due to the deviations  
29  
30  
31 in the surface morphology of Q/Bi<sub>2</sub>Se<sub>3</sub>/ZnO samples.  
32  
33  
34  
35  
36  
37

38 Analysis of the defect emission peaks related to different types of defects for the  
39  
40  
41 G/Bi<sub>2</sub>Se<sub>3</sub>/ZnO heterostructures revealed that the linear enhancement of the summarized defect  
42  
43  
44 PL with the increase of the ZnO thickness (Figure 6h) is governed mostly by the defect peak  
45  
46  
47 related to the neutral zinc interstitials ( $\sim 3.11$  eV), which intensity increases linearly with the  
48  
49  
50 increase of ZnO nanolayer thickness (Figure 6 i). The intensities of other three peaks ( $\sim 1.96$   
51  
52  
53  
54

1  
2  
3 eV, ~2.23 eV and ~2.5 eV) of the defect emission of ZnO nanolayers increase with the increase  
4  
5  
6  
7 of ZnO thickness from 10 to 75 nm, and then decrease/saturate for the ZnO thicknesses above  
8  
9  
10 75 nm (Figure 6j) in all samples. Also, it is seen from the Figure 6j that the defect PL of these  
11  
12  
13 emission peaks in G/Bi<sub>2</sub>Se<sub>3</sub>/ZnO and Q/Bi<sub>2</sub>Se<sub>3</sub>/ZnO samples is higher than PL of the Si/ZnO  
14  
15  
16 samples. Presumably, this enhancement of the defect ZnO PL in Bi<sub>2</sub>Se<sub>3</sub>/ZnO heterostructures  
17  
18  
19 is promoted by the decrease of the depletion layer in comparison to the ZnO films deposited on  
20  
21  
22 Si substrates.<sup>14,31</sup> Additionally, the increase of the defect emission intensity for the ZnO  
23  
24  
25 thicknesses below 75 nm may be related to the higher concentration of the single-ionized  
26  
27  
28 oxygen and zinc vacancies (~2.5 eV). As it is known, these defects are concentrated on the  
29  
30  
31 ZnO grain boundaries. As the ZnO grain size decreases with the decrease of the ZnO nanolayer  
32  
33  
34 thickness (Figure 6k), the thinner ZnO nanolayers may have higher concentration of defects.  
35  
36  
37  
38 The dependence of the defect PL on ZnO grain size may explain also the higher defect PL of  
39  
40  
41 the ZnO in the Q/Bi<sub>2</sub>Se<sub>3</sub>/ZnO heterostructures in comparison with the G/Bi<sub>2</sub>Se<sub>3</sub>/ZnO (Figures 6j  
42  
43  
44 and 6k). The growth of the ZnO films above 75 nm is supported by the decrease of the defect  
45  
46  
47  
48  
49  
50  
51  
52  
53  
54  
55  
56  
57  
58  
59  
60

1  
2  
3 concentration due to the increase of the grain size and the improvement of crystalline structure  
4  
5  
6  
7 of the nanolayer,<sup>31</sup> which results in saturation of the defect PL.  
8  
9  
10  
11  
12

## 13 CONCLUSIONS

14  
15  
16  
17  $\text{Bi}_2\text{Se}_3/\text{ZnO}$  heterostructures with different structure properties have been fabricated using  
18  
19  
20 consecutive physical vapor deposition and atomic layer deposition techniques. Improvement of  
21  
22  
23 the crystalline structure of ZnO nanolayers grown by ALD method on Q/ $\text{Bi}_2\text{Se}_3$  and G/ $\text{Bi}_2\text{Se}_3$   
24  
25  
26 nanostructured substrates was observed comparing to the ZnO nanolayers grown by ALD on  
27  
28  
29 Si substrates. Significant enhancement of the band-edge emission of ZnO in  $\text{Bi}_2\text{Se}_3/\text{ZnO}$   
30  
31  
32 heterostructures was observed. Three main mechanisms of the PL improvement are proposed:  
33  
34  
35 (i) decrease of the depletion layer due to the charge transfer at the  $\text{Bi}_2\text{Se}_3/\text{ZnO}$  interface and  
36  
37  
38 formation of the hole-rich and electron-rich zones in  $\text{Bi}_2\text{Se}_3$  and ZnO respectively; (ii)  
39  
40  
41  
42 improvement of the ZnO crystallinity, especially in the ZnO nanolayers in G/ $\text{Bi}_2\text{Se}_3/\text{ZnO}$   
43  
44  
45  
46 heterostructures, and (iii) resonance of ZnO excitons with  $\text{Bi}_2\text{Se}_3$  surface plasmon polaritons at  
47  
48  
49 the  $\text{Bi}_2\text{Se}_3/\text{ZnO}$  interface. Analysis of the defect PL revealed its dependence on the width of the  
50  
51  
52  
53  
54  
55  
56  
57  
58  
59  
60

1  
2  
3 depletion layer and the average grain size of the ZnO. Bi<sub>2</sub>Se<sub>3</sub> and ZnO showed good  
4  
5  
6 compatibility of both Q/Bi<sub>2</sub>Se<sub>3</sub>/ZnO and G/Bi<sub>2</sub>Se<sub>3</sub>/ZnO heterostructures and their high potential  
7  
8  
9  
10 for applications in optoelectronic devices.  
11  
12  
13

## 14 ACKNOWLEDGEMENTS

15  
16  
17  
18  
19 This work was funded by the ERDF project No. 1.1.1.1/16/A/257, Taiwan–Latvia–Lithuania  
20  
21  
22 Cooperation Project LV–LT–TW/2019/1 and the European Union’s Horizon 2020 research and  
23  
24  
25 innovation program under grant agreement No: 778157 – CanBioSe.  
26  
27  
28  
29

30 Work related to TEM studies was performed at the Center for Integrated Nanotechnologies, an  
31  
32  
33 Office of Science User Facility operated for the U.S. Department of Energy (DOE) Office of  
34  
35  
36 Science. Los Alamos National Laboratory, an affirmative action equal opportunity employer, is  
37  
38  
39 managed by Triad National Security, LLC for the U.S. Department of Energy’s NNSA, under  
40  
41  
42  
43 contract 89233218CNA000001.  
44  
45  
46  
47

48 CORRESPONDING AUTHOR.

49  
50  
51  
52  
53 \*E-mail: [donats.erts@lu.lv](mailto:donats.erts@lu.lv)  
54  
55

## REFERENCES.

- (1) Özgür, Ü.; Alivov, Y. I.; Liu, C.; Teke, A.; Reshchikov, M. A.; Doğan, S.; Avrutin, V.; Cho, S. J.; Morkoç, H. A Comprehensive Review of ZnO Materials and Devices. *J. Appl. Phys.* **2005**, *98*, 041301.
- (2) Son, D. I.; Kwon, B. W.; Park, D. H.; Seo, W. S.; Yi, Y.; Angadi, B.; Lee, C. L.; Choi, W. K. Emissive ZnO-Graphene Quantum Dots for White-Light-Emitting Diodes. *Nat. Nanotechnol.* **2012**, *7*, 465–471.
- (3) Liang, Y. C.; Zhao, Q.; Liu, K. K.; Liu, Q.; Lu, X. L.; Wu, X. Y.; Lu, Y. J.; Dong, L.; Shan, C. X. Ultrasensitive Mechano-Stimuli Luminescence Enhancement in ZnO Nanoparticles. *J. Phys. Chem. Lett.* **2019**, *10*, 3557–3562.
- (4) Chaaya, A. A.; Bechelany, M.; Balme, S.; Miele, P. ZnO 1D Nanostructures Designed by Combining Atomic Layer Deposition and Electrospinning for UV Sensor Applications. *J. Mater. Chem. A* **2014**, *2*, 20650–20658.
- (5) Ning, Y.; Zhang, Z.; Teng, F.; Fang, X. Novel Transparent and Self-Powered UV

- 1  
2  
3 Photodetector Based on Crossed ZnO Nanofiber Array Homojunction. *Small* **2018**, *14*,  
4  
5  
6  
7 1703754.  
8  
9  
10  
11 (6) Zhao, B.; Wang, F.; Chen, H.; Zheng, L.; Su, L.; Zhao, D.; Fang, X. An Ultrahigh  
12  
13  
14 Responsivity ( $9.7 \text{ MA W}^{-1}$ ) Self-Powered Solar-Blind Photodetector Based on Individual  
15  
16  
17 ZnO–Ga<sub>2</sub>O<sub>3</sub> Heterostructures. *Adv. Funct. Mater.* **2017**, *27*, 1700264.  
18  
19  
20  
21  
22 (7) Zhang, Z.; Ning, Y.; Fang, X. From Nanofibers to Ordered ZnO/NiO Heterojunction Arrays  
23  
24  
25  
26 for Self-Powered and Transparent UV Photodetectors. *J. Mater. Chem. C* **2019**, *7*, 223–  
27  
28  
29 229.  
30  
31  
32  
33  
34 (8) Yuan, J.; Hu, L.; Xu, Z.; Zhang, Y.; Li, H.; Cao, X.; Liang, H.; Ruan, S.; Zeng, Y. J.  
35  
36  
37 Concurrent Improvement of Photocarrier Separation and Extraction in ZnO Nanocrystal  
38  
39  
40 Ultraviolet Photodetectors. *J. Phys. Chem. C* **2019**, *123*, 14766–14773.  
41  
42  
43  
44  
45 (9) Ouyang, W.; Teng, F.; Jiang, M.; Fang, X. ZnO Film UV Photodetector with Enhanced  
46  
47  
48 Performance: Heterojunction with CdMoO<sub>4</sub> Microplates and the Hot Electron Injection  
49  
50  
51 Effect of Au Nanoparticles. *Small* **2017**, *13*, 1702177.  
52  
53  
54

- 1  
2  
3  
4 (10) Ahn, M. W.; Park, K. S.; Heo, J. H.; Kim, D. W.; Choi, K. J.; Park, J. G. On-Chip  
5  
6  
7 Fabrication of ZnO-Nanowire Gas Sensor with High Gas Sensitivity. *Sensors Actuators,*  
8  
9  
10 *B Chem.* **2009**, *138*, 168–173.  
11  
12  
13  
14 (11) Tamashevski, A.; Harmaza, Y.; Viter, R.; Jevdokimovs, D.; Poplausks, R.; Slobozhanina,  
15  
16  
17 E.; Mikoliunaite, L.; Erts, D.; Ramanaviciene, A.; Ramanavicius, A. Zinc Oxide Nanorod  
18  
19  
20 Based Immunosensing Platform for the Determination of Human Leukemic Cells. *Talanta*  
21  
22  
23 **2019**, *200*, 378–386.  
24  
25  
26  
27  
28  
29 (12) Viter, R.; Savchuk, M.; Starodub, N.; Balevicius, Z.; Tumenas, S.; Ramanaviciene, A.;  
30  
31  
32 Jevdokimovs, D.; Erts, D.; Iatsunskiy, I.; Ramanavicius, A. Photoluminescence  
33  
34  
35 Immunosensor Based on Bovine Leukemia Virus Proteins Immobilized on the ZnO  
36  
37  
38 Nanorods. *Sensors Actuators, B Chem.* **2019**, *285*, 601–606.  
39  
40  
41  
42  
43  
44 (13) Weber, M.; Julbe, A.; Ayral, A.; Miele, P.; Bechelany, M. Atomic Layer Deposition for  
45  
46  
47 Membranes: Basics, Challenges, and Opportunities. *Chem. Mater.* **2018**, *30*, 7368–7390.  
48  
49  
50  
51  
52 (14) Chaaya, A. A.; Viter, R.; Baleviciute, I.; Bechelany, M.; Ramanavicius, A.; Gertnere, Z.;  
53  
54  
55

- 1  
2  
3 Erts, D.; Smyntyna, V.; Miele, P. Tuning Optical Properties of Al<sub>2</sub>O<sub>3</sub>/ZnO Nanolaminates  
4  
5  
6  
7 Synthesized by Atomic Layer Deposition. *J. Phys. Chem. C* **2014**, *118*, 3811–3819.  
8  
9  
10  
11 (15) Viter, R.; Abou Chaaya, A.; Iatsunskyi, I.; Nowaczyk, G.; Kovalevskis, K.; Erts, D.; Miele,  
12  
13 P.; Smyntyna, V.; Bechelany, M. Tuning of ZnO 1D Nanostructures by Atomic Layer  
14  
15 Deposition and Electrospinning for Optical Gas Sensor Applications. *Nanotechnology*  
16  
17  
18 **2015**, *26*, 105501.  
19  
20  
21  
22  
23  
24  
25  
26 (16) Viter, R.; Iatsunskyi, I.; Fedorenko, V.; Tumenas, S.; Balevicius, Z.; Ramanavicius, A.;  
27  
28  
29 Balme, S.; Kempniński, M.; Nowaczyk, G.; Jurga, S.; et al. Enhancement of Electronic and  
30  
31  
32 Optical Properties of ZnO/Al<sub>2</sub>O<sub>3</sub> Nanolaminate Coated Electrospun Nanofibers. *J. Phys.*  
33  
34  
35  
36  
37 *Chem. C* **2016**, *120*, 5124–5132.  
38  
39  
40  
41 (17) Baitimirova, M.; Viter, R.; Andzane, J.; Van Der Lee, A.; Voiry, D.; Iatsunskyi, I.; Coy, E.;  
42  
43  
44 Mikoliunaite, L.; Tumenas, S.; Zaleski, K.; et al. Tuning of Structural and Optical  
45  
46  
47 Properties of Graphene/ZnO Nanolaminates. *J. Phys. Chem. C* **2016**, *120*, 23716–23725.  
48  
49  
50  
51  
52 (18) Iatsunskyi, I.; Baitimirova, M.; Coy, E.; Yate, L.; Viter, R.; Ramanavicius, A.; Jurga, S.;  
53  
54  
55  
56  
57  
58  
59  
60

- 1  
2  
3 Bechelany, M.; Erts, D. Influence of ZnO/Graphene Nanolaminate Periodicity on Their  
4  
5  
6  
7 Structural and Mechanical Properties. *J. Mater. Sci. Technol.* **2018**, *34*, 1487–1493.  
8  
9  
10  
11 (19) Bera, S.; Ghosh, S.; Basu, R. N. Fabrication of Bi<sub>2</sub>S<sub>3</sub>/ZnO Heterostructures: An Excellent  
12  
13  
14 Photocatalyst for Visible-Light-Driven Hydrogen Generation and Photoelectrochemical  
15  
16  
17  
18 Properties. *New J. Chem.* **2018**, *42*, 541–554.  
19  
20  
21  
22 (20) Xia, Y.; Qian, D.; Hsieh, D.; Wray, L.; Pal, A.; Lin, H.; Bansil, A.; Grauer, D.; Hor, Y. S.;  
23  
24  
25  
26 Cava, R. J.; et al. Observation of a Large-Gap Topological-Insulator Class with a Single  
27  
28  
29 Dirac Cone on the Surface. *Nat. Phys.* **2009**, *5*, 398–402.  
30  
31  
32  
33 (21) Andzane, J.; Kunakova, G.; Charpentier, S.; Hrkac, V.; Kienle, L.; Baitimirova, M.; Bauch,  
34  
35  
36  
37 T.; Lombardi, F.; Erts, D. Catalyst-Free Vapour-Solid Technique for Deposition of Bi<sub>2</sub>Te<sub>3</sub>  
38  
39  
40  
41 and Bi<sub>2</sub>Se<sub>3</sub> Nanowires/Nanobelts with Topological Insulator Properties. *Nanoscale* **2015**,  
42  
43  
44  
45 *7*, 15935–15944.  
46  
47  
48 (22) Xiu, F.; He, L.; Wang, Y.; Cheng, L.; Chang, L. Te; Lang, M.; Huang, G.; Kou, X.; Zhou,  
49  
50  
51  
52 Y.; Jiang, X.; et al. Manipulating Surface States in Topological Insulator Nanoribbons.  
53  
54

- 1  
2  
3  
4 *Nat. Nanotechnol.* **2011**, *6*, 216–221.  
5  
6  
7  
8 (23) Kunakova, G.; Galletti, L.; Charpentier, S.; Andzane, J.; Erts, D.; Léonard, F.; Spataru,  
9  
10  
11 C. D.; Bauch, T.; Lombardi, F. Bulk-Free Topological Insulator Bi<sub>2</sub>Se<sub>3</sub> Nanoribbons with  
12  
13  
14 Magnetotransport Signatures of Dirac Surface States. *Nanoscale* **2018**, *10*, 19595–  
15  
16  
17  
18 19602.  
19  
20  
21  
22 (24) Liao, Z. M.; Han, B. H.; Wu, H. C.; Yashina, L. V.; Yan, Y.; Zhou, Y. B.; Bie, Y. Q.; Bozhko,  
23  
24  
25  
26 S. I.; Fleischer, K.; Shvets, I. V.; et al. Surface Plasmon on Topological Insulator/Dielectric  
27  
28  
29 Interface Enhanced ZnO Ultraviolet Photoluminescence. *AIP Adv.* **2012**, *2*, 022105.  
30  
31  
32  
33 (25) Hong, S. S.; Cha, J. J.; Kong, D.; Cui, Y. Ultra-Low Carrier Concentration and Surface-  
34  
35  
36  
37 Dominant Transport in Antimony-Doped Bi<sub>2</sub>Se<sub>3</sub> Topological Insulator Nanoribbons. *Nat.*  
38  
39  
40  
41 *Commun.* **2012**, *3*, 757.  
42  
43  
44  
45 (26) Baitimirova, M.; Andzane, J.; Petersons, G.; Meija, R.; Poplausks, R.; Romanova, M.;  
46  
47  
48 Erts, D. Vapor–Solid Synthesis and Enhanced Thermoelectric Properties of Non-Planar  
49  
50  
51  
52 Bismuth Selenide Nanoplates on Graphene Substrate. *J. Mater. Sci.* **2016**, *51*, 8224–  
53  
54

- 1  
2  
3  
4 8232.  
5  
6  
7  
8 (27) Mattevi, C.; Kim, H.; Chhowalla, M. A Review of Chemical Vapour Deposition of  
9  
10  
11 Graphene on Copper. *J. Mater. Chem.* **2011**, *21*, 3324-3334.  
12  
13  
14  
15 (28) Ghoneim, M. T.; Smith, C. E.; Hussain, M. M. Simplistic Graphene Transfer Process and  
16  
17  
18  
19 Its Impact on Contact Resistance. *Appl. Phys. Lett.* **2013**, *102*, 183115.  
20  
21  
22  
23 (29) Andzane, J.; Britala, L.; Kauranens, E.; Neciporenko, A.; Baitimirova, M.; Lara-Avila, S.;  
24  
25  
26  
27 Kubatkin, S.; Bechelany, M.; Erts, D. Effect of Graphene Substrate Type on Formation of  
28  
29  
30  
31  $\text{Bi}_2\text{Se}_3$  Nanoplates. *Sci. Rep.* **2019**, *9*, 4791.  
32  
33  
34  
35 (30) Andzane, J.; Buks, K.; Strakova, M. N.; Zubkins, M.; Bechelany, M.; Marnauza, M.;  
36  
37  
38  
39 Baitimirova, M.; Erts, D. Structure and Doping Determined Thermoelectric Properties of  
40  
41  
42  
43  $\text{Bi}_2\text{Se}_3$  Thin Films Deposited by Vapour-Solid Technique. *IEEE Trans. Nanotechnol.*  
44  
45  
46  
47  
48  
49  
50 (31) Chaaya, A. A.; Viter, R.; Bechelany, M.; Alute, Z.; Erts, D.; Zaleskaya, A.; Kovalevskis,  
51  
52  
53  
54  
55  
56  
57  
58  
59  
60

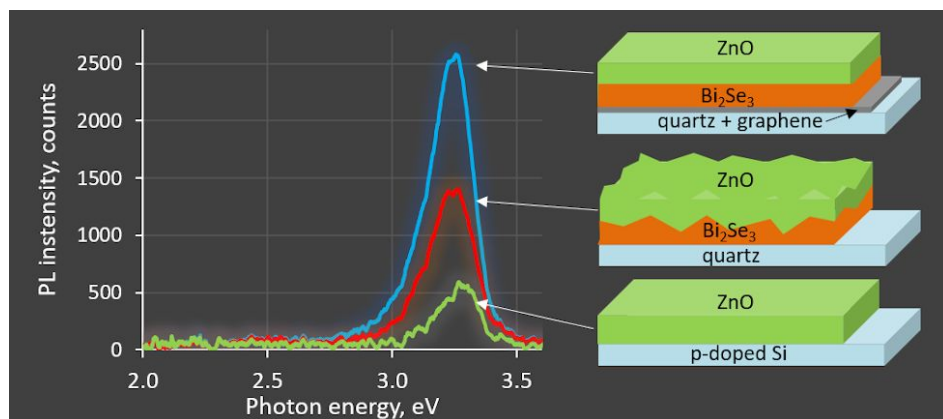
- 1  
2  
3  
4 Properties of ZnO Grown by Atomic Layer Deposition. *Beilstein J. Nanotechnol.* **2013**, *4*,  
5  
6  
7 690–698.  
8  
9  
10  
11 (32) Benchaabane, A.; Ben Hamed, Z.; Kouki, F.; Abderrahmane Sanhoury, M.; Zellama, K.;  
12  
13  
14 Zeinert, A.; Bouchriha, H. Performances of Effective Medium Model in Interpreting Optical  
15  
16  
17 Properties of Polyvinylcarbazole:ZnSe Nanocomposites. *J. Appl. Phys.* **2014**, *115*,  
18  
19  
20  
21 134313.  
22  
23  
24  
25  
26 (33) Ding, Z.; Bux, S. K.; King, D. J.; Chang, F. L.; Chen, T. H.; Huang, S. C.; Kaner, R. B.  
27  
28  
29 Lithium Intercalation and Exfoliation of Layered Bismuth Selenide and Bismuth Telluride.  
30  
31  
32  
33 *J. Mater. Chem.* **2009**, *19*, 2588–2592.  
34  
35  
36  
37 (34) Calestani, G. Introduction to Crystallography. *Adv. Imag. Elect. Phys.* **2002**, *123*, 29-70.  
38  
39  
40  
41 (35) Bindu, P.; Thomas, S. Estimation of Lattice Strain in ZnO Nanoparticles: X-Ray Peak  
42  
43  
44  
45 Profile Analysis. *J. Theor. Appl. Phys.* **2014**, *8*, 123–134.  
46  
47  
48  
49 (36) R. Saleh, W.; M. Saeed, N.; A. Twej, W.; Alwan, M. Synthesis Sol-Gel Derived Highly  
50  
51  
52  
53 Transparent ZnO Thin Films for Optoelectronic Applications. *Adv. Mater. Phys. Chem.*  
54  
55

- 1  
2  
3  
4       **2012, 02, 11–16.**  
5  
6  
7  
8       (37) Liang, W. Y.; Yoffe, A. D. Transmission Spectra of ZnO Single Crystals. *Phys. Rev. Lett.*  
9  
10  
11       **1968, 20, 59–62.**  
12  
13  
14  
15       (38) Arif, A.; Belahssen, O.; Gareh, S.; Benramache, S. The Calculation of Band Gap Energy  
16  
17       in Zinc Oxide Films. *J. Semicond.* **2015, 36, 013001.**  
18  
19  
20  
21  
22  
23       (39) Fang, J.; Fan, H.; Ma, Y.; Wang, Z.; Chang, Q. Surface Defects Control for ZnO Nanorods  
24  
25       Synthesized by Quenching and Their Anti-Recombination in Photocatalysis. *Appl. Surf.*  
26  
27       *Sci.* **2015, 332, 47–54.**  
28  
29  
30  
31  
32  
33  
34       (40) Antony, A.; Poornesh, P.; Kityk, I. V.; Myronchuk, G.; Sanjeev, G.; Petwal, V. C.; Verma,  
35  
36       V. P.; Dwivedi, J. A Study of 8 MeV E-Beam on Localized Defect States in ZnO  
37  
38       Nanostructures and Its Role on Photoluminescence and Third Harmonic Generation. *J.*  
39       *Lumin.* **2019, 207, 321–332.**  
40  
41  
42  
43  
44  
45  
46  
47  
48  
49       (41) Janotti, A.; Van De Walle, C. G. Fundamentals of Zinc Oxide as a Semiconductor.  
50  
51       *Reports Prog. Phys.* **2009, 72, 126501.**  
52  
53  
54

- 1  
2  
3  
4 (42) Janotti, A.; Van De Walle, C. G. Native Point Defects in ZnO. *Phys. Rev. B* **2007**, *76*,  
5  
6  
7 165202.  
8  
9  
10  
11 (43) Edmonds, M. T.; Hellerstedt, J. T.; Tadich, A.; Schenk, A.; Donnell, K. M. O.; Tosado, J.;  
12  
13  
14 Butch, N. P.; Syers, P.; Paglione, J.; Fuhrer, M. S. Stability and Surface Reconstruction  
15  
16  
17 of Topological Insulator Bi<sub>2</sub>Se<sub>3</sub> on Exposure to Atmosphere. *J. Phys. Chem. C* **2014**, *118*,  
18  
19  
20  
21 20413-20419.  
22  
23  
24  
25  
26 (44) Edmonds, M. T.; Hellerstedt, J. T.; Tadich, A.; Schenk, A.; O'Donnell, K. M.; Tosado, J.;  
27  
28  
29 Butch, N. P.; Syers, P.; Paglione, J.; Fuhrer, M. S. Air-Stable Electron Depletion of Bi<sub>2</sub>Se<sub>3</sub>  
30  
31  
32 Using Molybdenum Trioxide into the Topological Regime. *ACS Nano* **2014**, *8*, 6400–  
33  
34  
35  
36 6406.  
37  
38  
39  
40  
41 (45) Spataru, C. D.; Léonard, F. Fermi-Level Pinning, Charge Transfer, and Relaxation of  
42  
43  
44 Spin-Momentum Locking at Metal Contacts to Topological Insulators. *Phys. Rev. B* **2014**,  
45  
46  
47  
48 *90*, 085115.  
49  
50  
51  
52 (46) Reshchikov, M. A.; Behrends, A.; Bakin, A.; Waag, A. Photoluminescence from ZnO  
53  
54

1  
2  
3 Nanowires. *J. Vac. Sci. Technol. B Microelectron. Nanom. Struct.* 2009, 27, 1688.  
4  
5  
6  
7  
8  
9  
10  
11  
12  
13  
14  
15

16 TOC figure.  
17  
18  
19



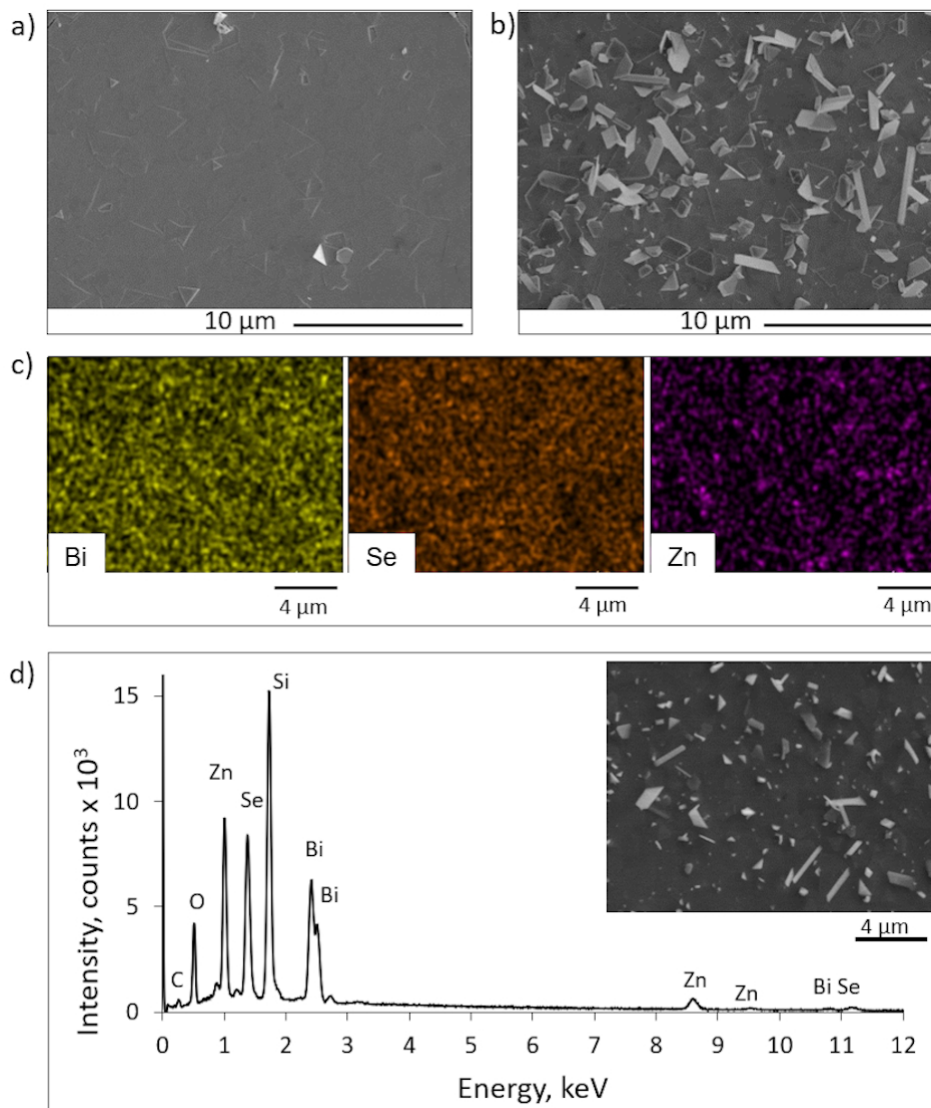


Figure 1. SEM images of  $\sim 110$ - $130$  nm thin Bi<sub>2</sub>Se<sub>3</sub> nanostructures covered with 50 nm thin ZnO nanolayer: a) G/Bi<sub>2</sub>Se<sub>3</sub>/ZnO heterostructure, b) Q/Bi<sub>2</sub>Se<sub>3</sub>/ZnO heterostructure, c) an example of SEM-EDX mapping, and d) EDX spectrum of fabricated Q/Bi<sub>2</sub>Se<sub>3</sub>/ZnO heterostructure.

84x95mm (300 x 300 DPI)

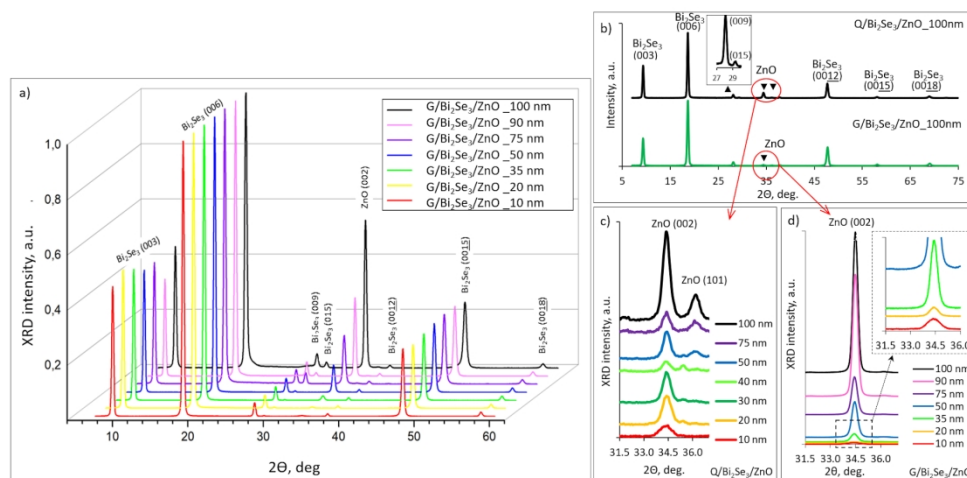


Figure 2. Full XRD spectra of a) G/Bi<sub>2</sub>Se<sub>3</sub>/ZnO heterostructures with ZnO nanolayers thicknesses 10-100 nm; b) G/Bi<sub>2</sub>Se<sub>3</sub>/ZnO (green) and Q/Bi<sub>2</sub>Se<sub>3</sub>/ZnO (black) heterostructures with ZnO nanolayer thickness 100 nm; c,d) enlarged images of the region of ZnO diffraction plane positions for the Q/Bi<sub>2</sub>Se<sub>3</sub>/ZnO (c) and G/Bi<sub>2</sub>Se<sub>3</sub>/ZnO (d and d, inset) heterostructures with different ZnO nanolayers thicknesses.

170x84mm (300 x 300 DPI)

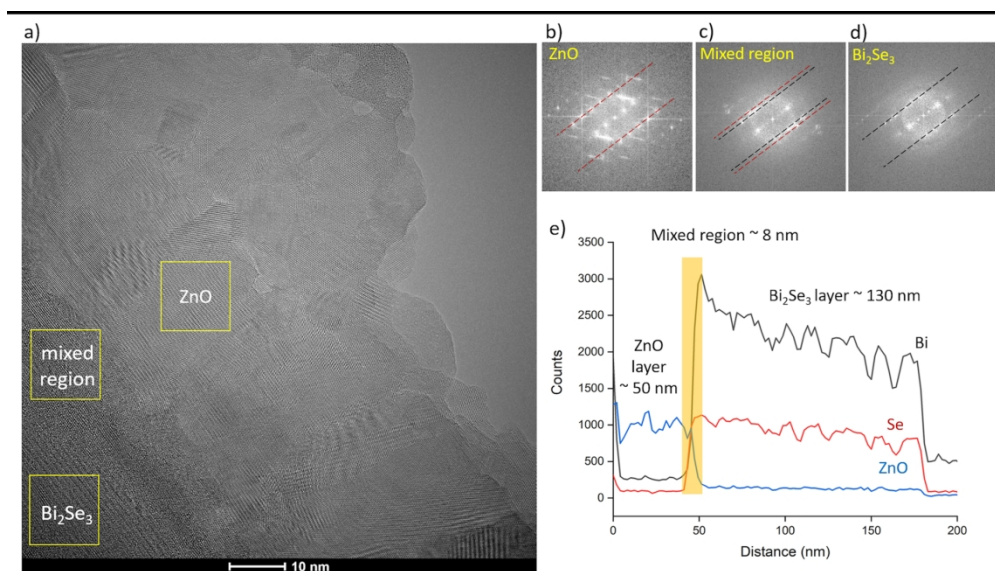


Figure 3. a) HRTEM image of the cross-section of Q/Bi<sub>2</sub>Se<sub>3</sub>/ZnO heterostructure with ZnO nanolayer thickness 50 nm; b-d) FFT images of ZnO, mixed region at the Bi<sub>2</sub>Se<sub>3</sub>/ZnO interface and Bi<sub>2</sub>Se<sub>3</sub>, taken from the areas of the sample labelled with squares at the HRTEM image; e) Line EDX scan of the cross-section of the Q/Bi<sub>2</sub>Se<sub>3</sub>/ZnO (50 nm) sample.

170x97mm (300 x 300 DPI)

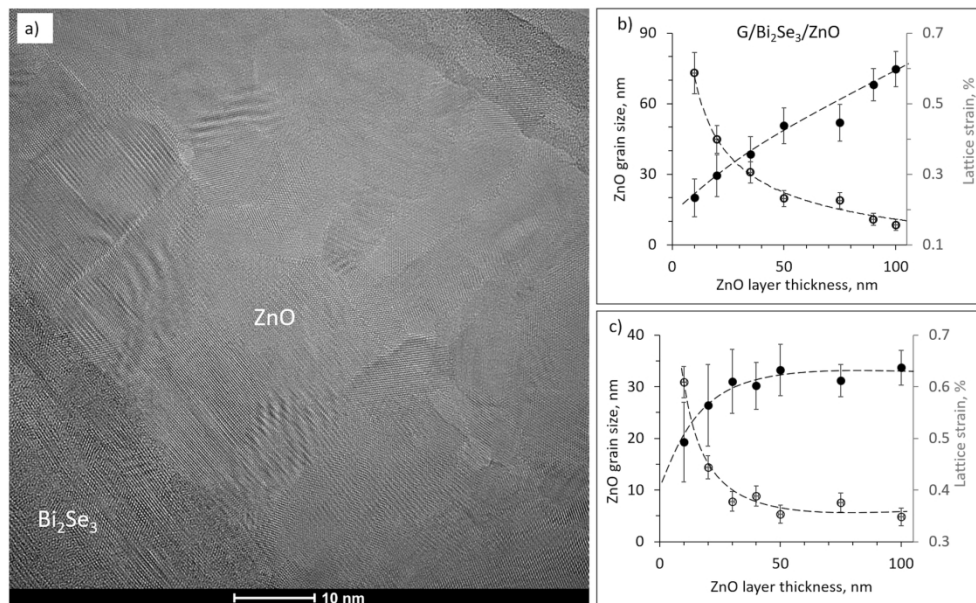


Figure 4. a) HRTEM image of the crosssection of Q/Bi<sub>2</sub>Se<sub>3</sub>/ZnO heterostructure (thickness of ZnO nanolayer 50 nm); b-c) Apparent ZnO grain size (primary y-axis, black circles) and lattice strain (secondary y-axis, hollow circles) vs ZnO nanolayers thickness in b) G/Bi<sub>2</sub>Se<sub>3</sub>/ZnO, and c) Q/Bi<sub>2</sub>Se<sub>3</sub>/ZnO heterostructures.

170x105mm (300 x 300 DPI)

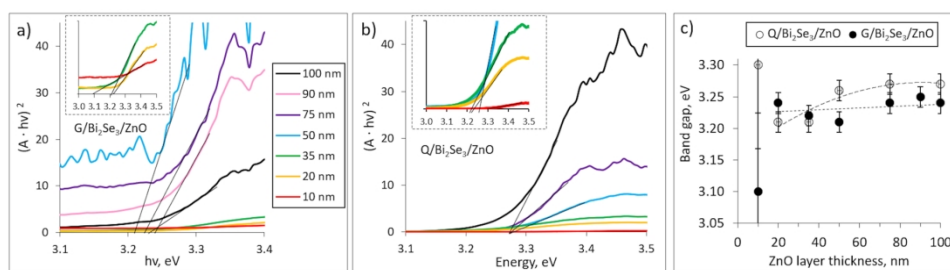


Figure 5. Band gap determination on the absorption edge from absorbance spectra for the ZnO nanolayers of different thicknesses in (a) G/Bi<sub>2</sub>Se<sub>3</sub>/ZnO and (b) Q/Bi<sub>2</sub>Se<sub>3</sub>/ZnO heterostructures; (c) Band gap values vs ZnO nanolayer thickness in Q/Bi<sub>2</sub>Se<sub>3</sub>/ZnO and G/Bi<sub>2</sub>Se<sub>3</sub>/ZnO heterostructures.

170x52mm (300 x 300 DPI)

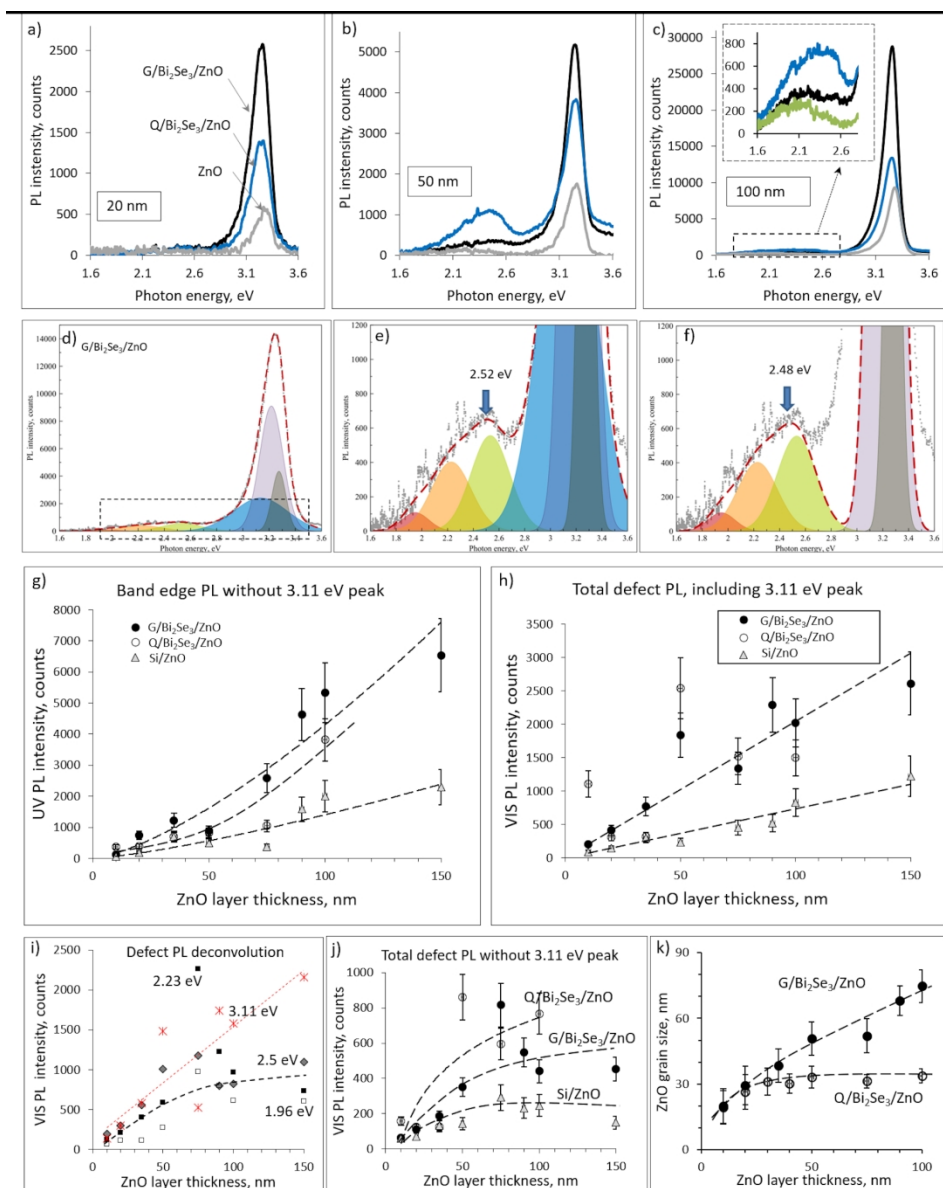


Figure 6. Photoluminescence spectra of Q/Bi<sub>2</sub>Se<sub>3</sub>/ZnO, G/Bi<sub>2</sub>Se<sub>3</sub>/ZnO heterostructures and for the comparison - of ZnO thin films with different ZnO nanolayer thicknesses: a) 20 nm, b) 50 nm, c) 100 nm; d) an example of deconvoluted G/Bi<sub>2</sub>Se<sub>3</sub>/ZnO spectrum; e) deconvolution of the defect emission peak; f) deconvolution of the defect emission peak without the contribution of the defect peak related to the neutral Zn vacancies; g) band edge PL intensities of the G/Bi<sub>2</sub>Se<sub>3</sub>/ZnO, Q/Bi<sub>2</sub>Se<sub>3</sub>/ZnO and Si/ZnO vs ZnO nanolayer thickness; h) defect ZnO emission intensities of the G/Bi<sub>2</sub>Se<sub>3</sub>/ZnO, Q/Bi<sub>2</sub>Se<sub>3</sub>/ZnO and Si/ZnO vs ZnO nanolayer thickness (with the contribution of 3.11 eV peak related to the neutral Zn vacancies); i) intensities of emission peaks related to different types of defects thickness for G/Bi<sub>2</sub>Se<sub>3</sub>/ZnO heterostructures vs ZnO nanolayer thickness; j) defect ZnO emission intensities (without the contribution of 3.11 eV peak related to the neutral Zn vacancies) of the G/Bi<sub>2</sub>Se<sub>3</sub>/ZnO, Q/Bi<sub>2</sub>Se<sub>3</sub>/ZnO and Si/ZnO vs ZnO nanolayer thickness and k) comparison between the ZnO grain sizes in G/Bi<sub>2</sub>Se<sub>3</sub>/ZnO and Q/Bi<sub>2</sub>Se<sub>3</sub>/ZnO vs ZnO thickness.

170x214mm (300 x 300 DPI)

1  
2  
3  
4  
5  
6  
7  
8  
9  
10  
11  
12  
13  
14  
15  
16  
17  
18  
19  
20  
21  
22  
23  
24  
25  
26  
27  
28  
29  
30  
31  
32  
33  
34  
35  
36  
37  
38  
39  
40  
41  
42  
43  
44  
45  
46  
47  
48  
49  
50  
51  
52  
53  
54  
55  
56  
57  
58  
59  
60

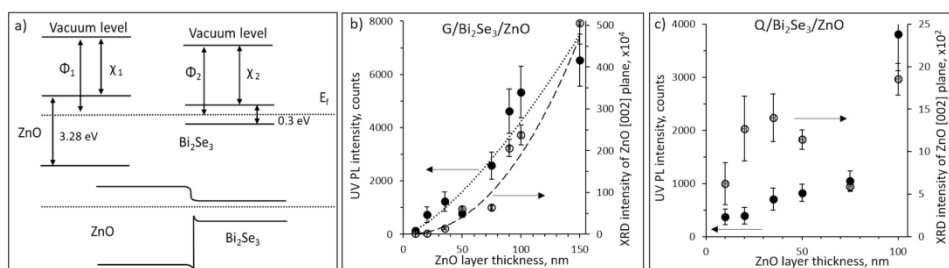
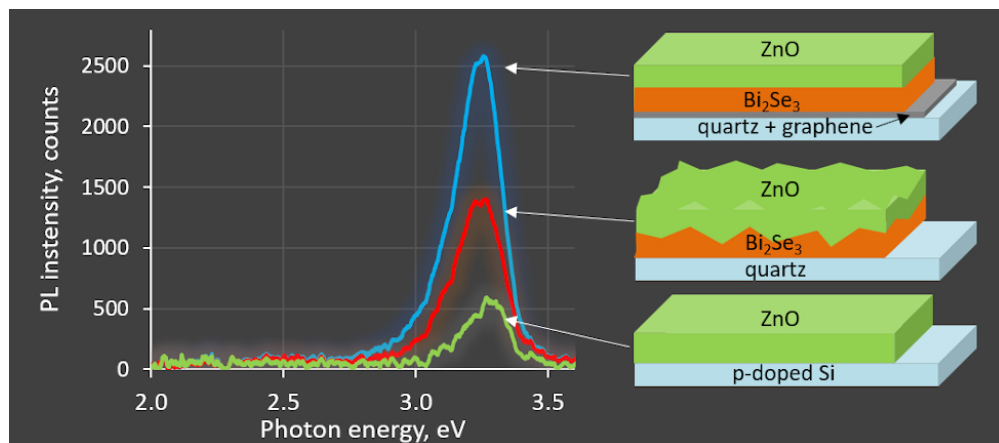


Figure 7. a) Band diagram for the Bi<sub>2</sub>Se<sub>3</sub>/ZnO interface. b,c) Dependence of ZnO PL intensity (primary y axis, black circles, dotted line) and XRD peak intensity (secondary y axis, hollow circles, dashed line) of G/Bi<sub>2</sub>Se<sub>3</sub>/ZnO (b) and Q/Bi<sub>2</sub>Se<sub>3</sub>/ZnO (c) heterostructures.

170x53mm (300 x 300 DPI)



TOC figure

82x36mm (300 x 300 DPI)